Volume 34 (2015), Number x pp. 0–24 COMPUTER GRAPHICS *forum*

Real-time Rendering Techniques with Hardware Tessellation

M. Nießner[1] and B. Keinert[2] and M. Fisher[1] and M. Stamminger[2] and C. Loop[3] and H. Schäfer[2]

[1]Stanford University [2]University of Erlangen-Nuremberg [3]Microsoft Research

Abstract

Graphics hardware has been progressively optimized to render more triangles with increasingly flexible shading. For highly detailed geometry, interactive applications restricted themselves to performing transforms on fixed geometry, since they could not incur the cost required to generate and transfer smooth or displaced geometry to the GPU at render time. As a result of recent advances in graphics hardware, in particular the GPU tessellation unit, complex geometry can now be generated on-the-fly within the GPU's rendering pipeline. This has enabled the generation and displacement of smooth parametric surfaces in real-time applications. However, many well-established approaches in offline rendering are not directly transferable due to the limited tessellation patterns or the parallel execution model of the tessellation stage. In this survey, we provide an overview of recent work and challenges in this topic by summarizing, discussing, and comparing methods for the rendering of smooth and highly-detailed surfaces in real-time.

1. Introduction

Graphics hardware originated with the goal of efficiently rendering geometric surfaces. GPUs achieve high performance by using a pipeline where large components are performed independently and in parallel. While a GPU may contain several thousand processing units [Nvi12a], the primary bottleneck has become the memory bandwidth between the processing units and the assets on the graphics card. This is a significant problem for real-time rendering applications, which seek to use increasingly complex and detailed geometry. For sufficiently detailed meshes, the memory cost to represent and dynamically animate the mesh as a raw collection of triangles rapidly becomes prohibitive. *Hardware tessellation* was introduced along with the Xbox 360 [AB06] and the Direct3D 11 API [Mic09] specifically to combat this problem. The main insight behind hardware tessellation is the generation of highly-detailed geometry on-the-fly from a coarser representation. Meshes are defined as a set of patch primitives, rather than a purely triangle-based representation. At run-time, patches are sent to the GPU streaming processors, where they are refined and subsequently rasterized without further memory I/O; Figure 1 shows an example rendering. Tessellations can adapt to the underlying surface complexity by programmable assignment of tessellation densities on a per-patch basis. Further geometric detail can be added on-the-fly by displacing generated vertices. This supports low-cost animations since only input patch control points need to be updated while displacement detail remains unchanged.

Hardware tessellation has attained widespread use in computer games for displaying highly-detailed, possibly animated, objects. In the animation industry, where displaced subdivision surfaces are the typical modeling and rendering primitive, hardware tessellation has also been identified as a useful technique for interactive modeling and fast previews. Much of the work presented in this report has been incorporated into `OpenSubdiv` [Pix12], an open source initiative

Figure 1: *Rendering from Unigine Heaven Benchmark with (right) and without (left) the use of hardware tessellation. While the base geometry is the same for both renderings, the highly-detailed geometry on the right is obtained by first tessellating the coarse mesh and using a displacement map.*

driven by Pixar Animation Studios, for use in games and authoring tools. In the near future, hardware tessellation will also be available on mobile devices [Nvi13, Qua13], opening the door for new applications in mobile graphics.

Although tessellation is a fundamental and well-researched problem in computer graphics, the availability of fast hardware tessellation has inspired researchers to develop techniques specifically crafted for hardware tessellation. This includes higher-order surface rendering methods that focus on different patch-based representations for the tessellator. Significant effort has been devoted to both accurately and approximately rendering subdivision surfaces. Hardware tessellation is also ideally suited for displacement mapping, where high-frequency geometric detail is efficiently encoded as image data and applied as surface offsets at run-time. Several approaches for incorporating such high-frequency details on top of smooth surfaces have been developed including methods for data storage, displacement evaluation, and smooth level-of-detail schemes. Additional research focuses on improving performance by avoiding the rendering of hidden patches; i.e., back-patch and occlusion culling. Further techniques address the handling of patch-based physics interactions such as collision detection for real-time rendering.

In this survey, we contribute a summary of such methods that are specifically designed for the GPU hardware tessellator and outline their contributions. In addition, we analyze and compare these approaches with respect to their usability and practicality for different scenarios. Note that this survey is the extended journal version of [SNK*14].

The techniques to be covered involve solutions for

- smooth surface rendering,
- low-cost animations and surface updates,
- adaptive level-of-detail,
- high-frequency detail; i.e., displacements,
- compact, consistent, and efficient texture storage,
- dynamic memory management for textures,
- fine-scale mesh deformations,
- culling techniques for faster rendering,
- tessellation-based collision detection.

Prior Hardware Tessellation Work Dynamic CPU-based tessellation methods are difficult to apply to real-time rendering, as the tessellated meshes must be transferred to the GPU continuously. As GPUs became more programmable, tessellation started being performed directly on the GPU, avoiding costly CPU-GPU data transfers. Vertex shaders made it possible to reposition vertices, so that the evaluation of vertex positions could be moved to the GPU, as long as a direct evaluation of the surface at a particular parameter position is possible. Geometry shaders can perform simple tessellation; however, they usually slow down the pipeline significantly, particularly if a single shader outputs a large number of triangles.

Boubekeur et al. [BS05,BS08] proposed the use of instantiation for tessellation. In their method, simple triangles are tessellated according to a set of tessellation factors, and are kept in GPU memory as so-called *tessellation patterns*. The tessellation patterns are then rendered using instantiation and applied to the patches of the base mesh. The requirement to keep patterns for all used tessellation factors results in a limited number of tessellation levels.

Later, methods to adaptively generate tessellation using GPGPU methods were presented. The hierarchical subdivision process is typically mapped to a parallel breadth-first traversal that successively generates smaller patches until they are considered to be fine enough [EML09, PEO09]. Schwarz et al. [SS09] parallelize the process patch-wise using a single thread per patch. This allowed them to use more efficient evaluation methods based on finite differences, but parallelization could only be exploited if a large number of single patches were subdivided and the subdivision levels did not vary largely. Other GPGPU-based approaches consider contour and silhouette information to perform adaptive mesh refinement while avoiding tessellation disparities [BA08], [FFB*09].

2. GPU Hardware Tessellation

2.1. Graphics Architectures

Modern GPUs are composed of several streaming multiprocessors (SMs) each of which is a vector processing unit. SMs process data chunks in parallel in a single-instruction-multiple-data (SIMD) fashion. The specific implementation of this kind of architecture is vendor-dependent. For example, NVIDIAs Kepler GK110 architecture [Nvi12b] consists of 15 streaming multiprocessors of which each unit features 192 single-precision cores resulting in a total number of 2880 cores. In this architecture, threads are dispatched by the streaming multiprocessors' schedulers in groups of 32 parallel threads called warps.

In contrast to conventional CPUs, GPUs spend more die area on computational units rather than on caches. While there is a small amount of shared memory available per SM (64 KB for the GK110) which can be used as L1 cache, most data must be obtained from global GPU memory. Access to global memory is costly, as it introduces high latency. Typically, latency is partially hidden by running a sufficient number of threads simultaneously and issuing computational instructions without requiring any memory accesses.

2.2. Graphics Pipeline and Hardware Tessellation

The typical graphics pipeline on current GPUs consists of five programmable shader stages (see Figure 2). GPUs can be programmed for rendering using the OpenGL or Direct3D API. Hardware tessellation has been accessible since Direct3D 11 [Mic09] and OpenGL Version 4.0 [SA12]. In the following, we will use the Direct3D nomenclature.

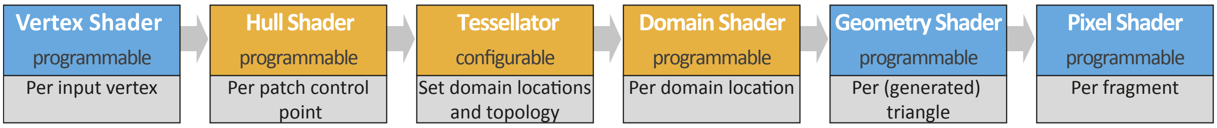

Figure 2: *Graphics pipeline according to Direct3D 11 nomenclature involving programmable shader and configurable hardware stages. For simplicity, the fixed-function stages input assembly, rasterization and output merger are omitted.*

Highly-tessellated meshes result in large memory footprints in GPU memory and are costly to render. In contrast, hardware tessellation allows for more output polygons since global memory access is only required for a sparse set of input control points. We benchmark this by generating 2 million output polygons on a planar grid using an NVIDIA GTX 780 graphics card. While conventional rendering using index and vertex buffers takes about 1.5 ms, using hardware tessellation takes only 0.25 ms; i.e., more efficient by a factor of ~ 6. However, enabling hardware tessellation *without* further tessellation of input patches is ineffective. That is, rendering the 2 million triangles with the tessellation unit and treating every triangle as a separate patch primitive with a tessellation factor of 1 is 5 times slower. Therefore, hardware tessellation should only be used where required; i.e., when the application necessitates further patch tessellation. Hardware tessellation elevates patch primitives to first class objects in the graphics pipeline. These patches are each defined by a set of control points, and processed in parallel by the GPU. The tessellation unit generates parameter sample values within corresponding patch domains where patches are evaluated. Currently, triangular, quadrilateral, and isoline domains are supported. Based on the tessellation configuration, patches are evaluated at the sample locations in order to generate an output stream composed of triangles. The key advantage is that these polygons are directly processed by the GPU streaming processors without involving further global memory access needed for vertex geometry data, thus minimizing memory I/O. This enables high-performance, dynamic patch tessellation.

Hardware tessellation introduces three new pipeline stages between vertex and geometry shading (see Figure 2): the hull shader stage, the tessellator stage and the domain shader stage. The hull shader stage is divided into two logical parts: a per-patch constant function and the actual hull shader program. The per-patch constant function is executed once per input patch and is used to determine the patch tessellation density. As such, per-patch tessellation factors are computed and sent to the fixed-function tessellator stage in order to specify the amount of generated domain sample points. For tri- and quad-domains there are edge (3 for tris, 4 for quads) and interior (1 for tris, 2 for quads) tessellation factors. The isoline domain is only controlled by two edge tessellation factors that determine the line density and the line detail. Aside from integer tessellation factors, fractional tessellation factors are also available, enabling smooth level-of-detail transitions. The hull shader program is executed for every patch control point. While one thread processes a single (output) control point, all patch input point data is shared among hull shader programs of the same patch. Currently, the number of control points is limited to 32 per patch.

The hull shader stage is followed by the fixed-function tessellator, generating sample points and topology for a given patch domain based on input tessellation factors. Examples of resulting tessellation patterns are shown in Figure 3, including tri- and quad-domains, as well as integer and fractional tessellation factors.

The last stage of the tessellation pipeline is the programmable domain shader stage where a shader program is invoked for each sample location. The input for this stage is composed of the hull shader output (i.e., tessellation factors, control points) and domain sample parameters. These are either barycentric coordinate triples *uvw* (tri-domain), or two-dimensional *uv* coordinates (quad and isoline domains). Based on the input, patches are evaluated, and an output vertex is generated for every domain sample. In addition, per-vertex attributes such as texture coordinates and surfaces normals must be computed and passed along with the posi-

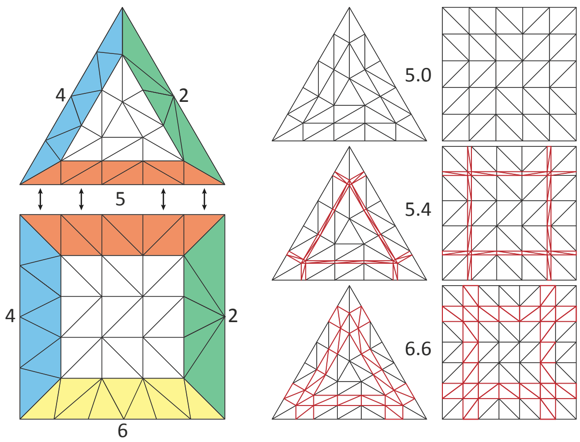

Figure 3: *Generated tessellation patterns of triangle and quad patch domains for different tessellation factors. Left: patches are uniformly tessellated in the interior (white) and support arbitrary tess factors on the edges resulting in transitional triangulation (colored) for watertight rendering of adjacent patches with different interior factors. Right: fractional tessellation enables smooth transitions between integer levels (fractional triangles red).*

tions of emitted vertices. These vertices are then triangulated using the topology generated by the fixed function tessellator and processed by the remaining stages of the graphics pipeline.

3. Higher-Order Surface Rendering

One of the main purposes of hardware tessellation is to support higher-order surface primitives, particularly parametric patches. A parametric patch is a mapping from a unit square or triangle (parameter) domain into 3D space. The precise nature of this mapping is specified by the programmer, both in terms of the assigned meaning of the input data, and the evaluation procedures executed by the hull and domain shader programs.

3.1. Bézier Patches

We start with a tensor product bi-cubic Bézier patch, written

$$P(u,v) \;=\; \sum_{i=0}^{3}\sum_{j=0}^{3} \mathbf{b}_{i,j} B_i^3(u) B_j^3(v), \tag{1}$$

where u,v are the coordinates of a point in a unit square domain $[0,1]\times[0,1]$, $\mathbf{b}_{i,j}$ are 16 three-dimensional *control points* that determine the shape of the patch, and $B_k^3(t)$ are Bernstein polynomials that are defined as

$$B_k^d(t) = \binom{d}{k}(1-t)^{d-k}t^k. \tag{2}$$

The 16 patch control points are transmitted to the GPU in a vertex buffer (either contiguously, or referenced by an index buffer). A hull shader program is executed once for each output vertex (in parallel).

3.1.1. Crack Avoidance

Bézier patches have the property that the 4 patch control points along the shared edges between pairs of patches must be identical to maintain a continuous, C^0 surface. In order to avoid cracks in a rendered surface, adjacent patches must be C^0. Furthermore, the tessellation factor must be assigned identically to the shared edge between a pair of adjacent patches; otherwise, the tessellation unit may not sample the shared patch boundary at corresponding parameter values of adjacent patches, leading to cracks. Sharing control point data and assigning identical tessellation factors along shared edges is necessary to avoid cracks, but it is not sufficient. Additionally, the domain shader program must take into account the different ordering of the control points with respect to the two patches sharing an edge. If it does not, then different numerical roundings may accumulate sufficiently to cause output vertices to project to different pixels, resulting in visible cracks between patches. The degree to which this matters is application dependent, but in many cases such cracks must be avoided to guarantee a high rendering quality.

Fortunately, it is relatively easy to evaluate the Bernstein basis in a *reversal invariant* way; i.e., independent of parameter direction. This can be achieved using the following procedure

```
void EvalBezCubic(float u, out float B[4]) {
  float T = u, S = 1.0 - u;

  B[0] = S*S*S;
  B[1] = 3.0*T*S*T;
  B[2] = 3.0*S*T*S;
  B[3] = T*T*T;
}
```

Note that replacing u by $1-u$ interchanges the values of S and T, leading to the reversal of basis function values. The boundary curve is evaluated by taking the dot product of the 4 boundary control points and these basis function values. Guaranteeing that the results are bitwise-identical on both sides of a shared boundary requires commutativity of both addition and multiplication. These commutativity requirements are satisfied by using IEEE floating point strictness when compiling shader programs.

While guaranteeing bitwise-identical geometry along shared patch boundaries is fairly straightforward using Bézier patches, guaranteeing bitwise-identical normals is not. The problem is that cross-boundary derivatives (e.g., the v direction, if u is along the boundary) may not be computed identically since they are constructed from different (non-shared) input data. This will result in slightly different normal vectors along a shared patch boundary. When used for lighting, the small color differences that might result may not be a problem. However, when used for displacement mapping, these differences will likely lead to visible cracks along patch boundaries. These problems are much easier to avoid by using the B-spline basis.

3.2. B-spline Patches

The B-spline basis has deep theoretical roots far beyond the scope of this report; we give B-splines only superficial treatment here. B-splines are a special case of the more general Non-Uniform Rational B-splines (NURBS), that are uniform and polynomial (non-rational).

A bi-cubic B-spline surface can be written as a piecewise mapping from a planar domain $[0,m+1]\times[0,n+1]$

$$P(u,v) \;=\; \sum_{i=0}^{m}\sum_{j=0}^{n} \mathbf{d}_{i,j} N^3(u-i) N^3(v-j), \tag{3}$$

where the $\mathbf{d}_{i,j}$ are a rectangular array of B-spline control points, and $N^3(t)$ is a cubic B-spline basis function. $N^3(t)$ is a C^2 smooth, piecewise cubic polynomial curve comprised of 4 non-zero curve segments. Since these basis functions are C^2 (curvature continuous), a linear combination of them is also C^2. This makes the construction of a curvature continuous surface easy.

Each individual cubic curve segment is determined by 4 contiguous control points, and each bi-cubic B-spline patch by 16 control points. A pair of adjacent curve segments will have 3 control points in common. Similarly, a pair of adjacent patches will have 12 control points in common. These 12 shared control points are exactly the ones needed to construct the positions and normals along the shared boundary.

3.3. Catmull-Clark Subdivision Surfaces

Catmull-Clark subdivision [CC78] is a generalization of bi-cubic B-spline subdivision to irregular control meshes. That is, a mesh with faces and vertices not incident on 4 edges (*extraordinary* vertices). By repeating the subdivision process, a smooth limit surface is obtained as shown in Figure 4.

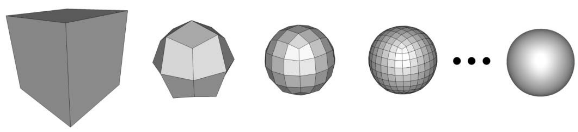

Figure 4: *Several iterations of Catmull-Clark subdivision applied to a cube-shaped base mesh.*

The algorithm is defined by a simple set of subdivision rules, which are used to create new face points (f_j), edge points (e_j) and vertex points (v_j) as a weighted average of points of the previous level mesh.

3.3.1. Subdivision Rules

The Catmull-Clark smooth subdivision rules for face, edge, and vertex points, as labeled in Figure 5, are defined as:

- Faces rule: f^{i+1} is the centroid of a face's vertices.
- Edge rule: $e^{i+1}_j = \frac{1}{4}(v^i + e^i_j + f^{i+1}_{j-1} + f^{i+1}_j)$,
- Vertex rule: $v^{i+1} = \frac{n-2}{n} v^i + \frac{1}{n^2}\sum_j e^i_j + \frac{1}{n^2}\sum_j f^{i+1}_j$.

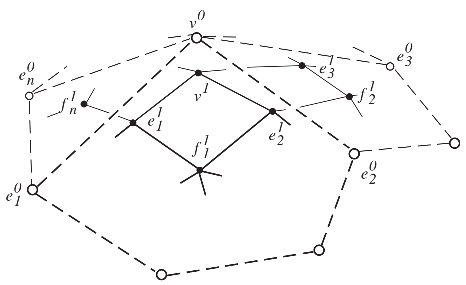

Figure 5: *Labeling of vertices of a Catmull-Clark [CC78] base mesh around the vertex v^0 of valence n.*

In the case that the input control mesh is locally regular, the resulting surface will locally be a bi-cubic B-spline. Additional refinements over these regions, while needed to refine the mesh, are not needed to determine the polynomial structure of the surface that is known once an individual B-spline patch has been determined. This patch structure is illustrated in Figure 7. We will see in Section 3.7 that this structure can be exploited using hardware tessellation for efficient rendering of the Catmull-Clark limit surface.

While subdivision surfaces freed designers from the topology constraints of B-splines, further development was needed to make them truly useful. For instance, the original subdivision rules did not consider the case of a mesh with boundary. Subsequent work took the idea a step further and allowed edges to have a variable amount of sharpness – called creases [HDD*94, DKT98].

3.4. Parallel Subdivision using GPU Kernels

As shown before, the rules for constructing new mesh points involve taking weighted averages of small, local collections of old mesh points. Gathering these points on the CPU usually involves neighborhood queries using a mesh connectivity data structure; e.g., winged-edge, half-edge, or quad-edge. While the details between these structures differ slightly, the basic idea is the same. Incidence relations are captured by linking edge data with pointers. In order to satisfy a neighborhood query (e.g., given a vertex, return all the vertices sharing an edge with the vertex in order), the connectivity structure must be traversed, one edge at a time, by following links and dereferencing pointers. Doing this on the GPU is impractical, due to the length and varying sizes of these edge chains.

3.4.1. Subdivision Tables

By assuming that mesh connectivity is static, or at least does not change often, a simple table-driven approach becomes feasible [NLMD12]. The idea is to encode the gather patterns of vertex indices, needed to construct new mesh points from old mesh points, and store these in tables. Since there are 3 types of new points being constructed in a Catmull-Clark subdivision surface (face, vertex, and edge), 3 compute kernels are used. Each compute kernel executes a single thread per new mesh point, and uses the indices stored in the tables to gather the old mesh vertices needed in the weighted average. Note that variations of table-driven subdivision have been used before general purposed computing was available on the GPU (e.g., [BS02]).

3.4.2. GPU Subdivision versus Hardware Tessellation

Given that subdivision on the GPU can be performed using tables, it may seem that patch-based hardware tessellation is not needed for rendering these primitives. One can simply transfer an unrestricted control cage to the GPU and let its massive data-parallelism generate and render millions of triangles. The problem with this idea is GPU memory bandwidth. Each level of the refined mesh must be streamed to and from the GPU and off-chip GPU memory. Each newly-generated level is roughly 4 times as large as the old level;

i.e., an exponential growth rate. While the table-driven approach efficiently maps the subdivision rules to the GPU, naïve use of this method will quickly become I/O bound. Hardware tessellation, on the other hand, is incredibly efficient since it avoids global (off-chip) memory accesses. Once a compact patch description is streamed to a local GPU cache, no further global memory accesses are needed. The hull, tessellation, domain, and even rasterization stages are all performed using fast, local GPU cache memory.

3.5. Stam's Algorithm

Stam [Sta98] proposed a method for the exact evaluation of Catmull-Clark Subdivision Surfaces. The advantage of Stam's algorithm is that it treats a subdivision surface as a parametric surface, which is seemingly ideal for hardware tessellation. In order to make the combinatorics tractable, Stam's algorithm requires that extraordinary vertices be isolated, so that no quadrilateral face is incident on more than one extraordinary. A face incident to a single extraordinary vertex, together with the vertices of all incident faces, is the input to Stam's algorithm; see Figure 6a. Let this collection of $2n+8$ vertices be labeled $\mathbf{v}_0$. With the resulting parameterization, all sub-patches can be enumerated

$$F_{j,k}(u,v) \;=\; N^3(u)N^3(v)\cdot P_j\cdot S^k\cdot \mathbf{v}_0, \qquad (4)$$

where $j=1,2,3$ is the index of a quad sub-domain (see Figure 6b), k is the level of subdivision, $N^3(t)$ is the cubic B-spline basis function, P_j is a *picking* matrix that generates the corresponding B-spline control points for the chosen patch, and S is the subdivision matrix whose entries correspond to the weights of the Catmull-Clark subdivision algorithm; for the details, we refer to [Sta98]. Performing the eigen decomposition of S, the patches are rewritten as

$$F_{j,k}(u,v) \;=\; \underbrace{N(u,v)\cdot P_j\cdot V}_{\text{eigen basis functions}}\cdot \Lambda^k\cdot \underbrace{V^{-1}\cdot \mathbf{v}_0}_{\text{eigen space projection}}\;, \qquad (5)$$

where V and V^{-1} are the left and right eigenvectors and Λ is the diagonal matrix of eigenvalues of S. Writing $F_{j,k}(u,v)$ this way shows that *subdivision*, or taking the matrix S to the k^{th} power, can be replaced by raising the diagonal elements of Λ to the k^{th} power. This requires substantially less computation, $O(c)$ operations per parametric evaluation. However, the constant c is rather large, due to the large number of floating point operations needed to evaluate the eigen basis functions and their derivatives. Further, Stam's algorithm does not handle sharp subdivision rules, and obtaining bitwise-exact boundary evaluation of positions and normals is problematic due to the eigen space projection.

3.6. Approximate Subdivision Methods

In order to maximize performance, researchers considered ways to render smooth higher-order surfaces that behave similarly to subdivision surfaces but are easier to evaluate.

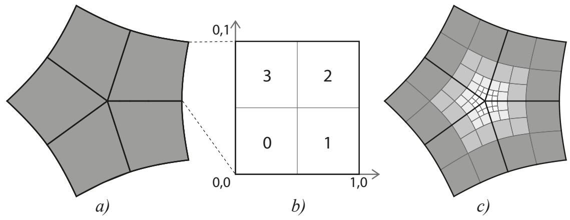

Figure 6: *a) Collection of control points input into Stam's algorithm. b) Labeling of corresponding sub-domains. c) Nesting of sub-domains around an extraordinary vertex.*

3.6.1. PN-triangles

The PN-triangle technique [VPBM01] was developed to add geometric fidelity to the large body of existing triangle mesh models. For each triangular face, a cubic Bézier triangle patch is constructed using only the position and normal data of the three incident vertices. A cubic Bézier triangle is determined by 10 control points. The position and normal at each vertex determines 3 control points that span the corresponding tangent planes. The final control is determined by a *quadratic precision* constraint; that is, if the 9 previously constructed control points happen to be consistent with a quadratic, then this 10^{th} control point will be consistent with the same quadratic. Note that this construction guarantees that a PN-triangle surface is continuous (C^0), but not smooth (C^1). To overcome this shortcoming, a PN-triangle contains a quadratic normal patch, whose coefficients are derived from the triangle's vertex normals. These normal patches, which are also continuous, are used for shading rather than the cubic geometry patch.

PN-triangles predate hardware tessellation, but their relatively simple and local construction is well suited to the hardware tessellation paradigm. A hull shader program can be used to convert a single mesh triangle and associated vertex data into a cubic geometry, and quadratic normal, patch pair. The domain shader stage will evaluate the cubic and quadratic input patches at their barycentric *uvw* coordinate triples. While PN-triangles are effective at improving the appearance of traditional triangle mesh models, they are not the best choice for obtaining results that approach the geometric quality of subdivision surfaces.

3.6.2. ACC-1: Approximation using Bézier Patches

Subdivision surfaces can be approximated based on quadrilateral bi-cubic patches [LS08]. Given a quad mesh as input, the idea is similar to PN-triangles in that a geometry patch is constructed to interpolate the position and tangent plane of the Catmull-Clark subdivision limit surface at the corners of a mesh quadrilateral. This bi-cubic patch, while designed to approximate the Catmull-Clark limit surface, will only be continuous, not smooth. Therefore, a *normal patch* is generated to create a smooth normal field for shading. As with PN-triangles, this algorithm is easily implemented in the hardware tessellation pipeline by using the hull shader for patch construction, and the domain shader for patch (geometry and normal) evaluation. Unlike PN-triangles, ACC-1 geometry and normal patches are both bi-cubic. This simplifies domain shader evaluation as only a single set of basis functions needs to be computed.

One of the advantages of approximating Catmull-Clark subdivision surfaces for hardware tessellation is that many authoring tools already exist for creating Catmull-Clark control cages for off-line applications like CG movies. The ACC-1 scheme made these tools available for real-time applications like games. However, professionally created subdivision models often employ crease and boundary rules. A full treatment of this issue in the context of ACC-1 patches appeared in [KMDZ09].

While the ACC-1 scheme is relatively fast, the requirement that patch control points be 6 dimensional (3 for position, 3 for surface normal), is not ideal and the underlying surface is not geometrically smooth. This led researchers to further develop approximate Catmull-Clark schemes. Several papers that split quad mesh faces into four triangles along both diagonals appeared [MNP08, MYP08, NYM*08]. These works generated smooth surfaces, but did so by increasing the patch count so that the effective throughput, the ratio of input control point data to output amplified geometry, went down. Ideally, we want large patches that are evaluated many times, thereby increasing this throughput.

3.6.3. ACC-2: Approximation using Gregory Patches

Constructing a piecewise smooth surface of arbitrary topological type from polynomial patches is a non-trivial problem. The difficulty lies in honoring the requirement that mixed partial derivatives ($\frac{\partial^2 F}{\partial uv} = \frac{\partial^2 F}{\partial vu}$) are consistent among patches at a shared extraordinary vertex. Adding degrees of freedom by domain splitting can be used to solve this problem (cf. ACC-1). Another approach is to use non-polynomial patches; this is the idea behind ACC-2 [LSNC09], a scheme based on *Gregory* patches [Gre74].

A bi-cubic Gregory patch is defined by 20 control points. Like a 16 control point bi-cubic Bézier patch, the 4 corner and 8 edge control points completely define the boundaries of the patch. The remaining interior control points are similar. However, each interior control point of a Bézier patch corresponds to two interior points of a Gregory patch. The reason for this is closely related to mixed partial derivatives. For a polynomial Bézier patch these must be equal (corresponding to a single interior control point per vertex). For non-polynomial Gregory patches, the mixed partial derivatives can disagree (hence the two interior control points per vertex). These additional degrees of freedom are used to solve the patch-to-patch smoothness constraints independently for Gregory patches, rather than as a (often times singular) system involving all patches incident on an extraordinary patch. The drawback to this approach is that the Gregory patch basis functions contain singularities ($\frac{0}{0}$) at corners. However, since we already know the limit position we want for these points, this issue causes no real concern in practice. The construction of ACC-2 control points is very similar to those for ACC-1.

To the best of our knowledge, the Gregory patch-based ACC-2 algorithm is the faster method for interpolating limit position corners and smoothly approximating the surface elsewhere. However, an artist who has painstakingly constructed a model using a Catmull-Clark subdivision surface is unlikely to be pleased if the renderer produced a slightly different result than intended. These differences are even more obvious when considering surface parameterization; however, He et al. [HLS12] presented a way to mitigate this to an extent. Artists and games developers would be much happier if the hardware tessellator could be used to render a Catmull-Clark subdivision surface accurately and efficiently.

3.7. Feature-Adaptive Subdivision

Feature-adaptive subdivision is a method for rendering Catmull-Clark limit surfaces with crease edge tags, that combines table-driven subdivision and hardware tessellation [NLMD12, Nie13]. As the term *feature-adaptive* implies, subdivision is only used where needed, to create as few bi-cubic patches as possible. These patches are then efficiently rendered using hardware tessellation. This algorithm has become the basis for Pixar's *OpenSubdiv* [Pix12], which is now used in major modeling packages.

It is well known that the limit surface defined by Catmull-Clark subdivision can be described by a collection of bi-cubic B-spline patches, where the set has infinitely many patches around extraordinary vertices, as illustrated in Figure 7(left). Similarly, near creases, the number of limit patches grows as the crease sharpness increases, as shown in Figure 7(right).

Feature-adaptive subdivision proceeds by identifying regular faces at each stage of subdivision, rendering each of these directly as a bi-cubic B-spline patch using hardware tessellation. Irregular faces are refined, and the process repeats at the next finer level. This strategy uses a table-driven approach; however, the subdivision tables are restricted to

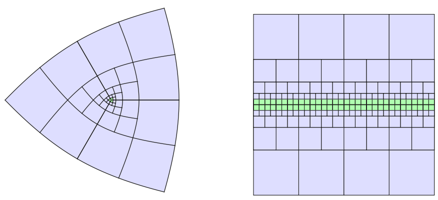

Figure 7: *The arrangement of bi-cubic patches (blue) around an extraordinary vertex (left), and near an infinitely sharp crease (right). Patches next to the respective feature (green) are irregular.*

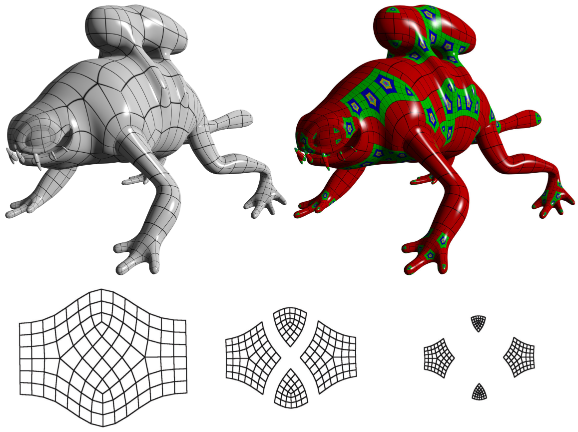

Figure 8: *The feature-adaptive subdivision scheme applied to the Monsterfrog model (top) and a grid with four extraordinary vertices (bottom). Subdivision is only performed in areas next to extraordinary vertices.*

irregular faces. A face is regular only if it is a quad with all regular vertices and if none of its edges or vertices are tagged as sharp. In all other cases the face is recognized as irregular, and subdivision tables are generated for a minimal number of subfaces. All of this analysis and table generation is done on the CPU at preprocessing time. Vertex and edge tagging is done at each level, depending on how many times the area around an irregular face should be subdivided. This might be the maximum desired subdivision depth around an extraordinary vertex, or the sharpness of a semi-sharp edge. As a result, each subdivision level will be a sequence of local control meshes that converge to the features of interest (see Figure 8).

3.7.1. Patch Construction

Once the subdivision stage is complete, the resulting patches are sent to the hardware tessellator for rendering. For each subdivision level there are two kinds of patches: full patches and transition patches.

3.7.2. Full Patches

Full patches (FPs) are patches that only share edges with patches of the same subdivision level. Regular FPs are passed through the hardware tessellation pipeline and rendered as bi-cubic B-splines. It is ensured by feature-adaptive subdivision that irregular FPs are only evaluated at patch corners. This means that for a given tessellation factor, $\lceil \log_2 \mathit{tessfactor} \rceil$ adaptive subdivision steps must be performed. Since current hardware supports a maximum tessellation factor of 64 ($= 2^6$), no more than 6 adaptive subdivision levels are required. In order to obtain the limit positions and tangents of patch corners of irregular FPs, a special vertex shader is used.

3.7.3. Transition Patches

Note that the arrangement of bi-cubic patches created by adaptive subdivision ensures that adjacent patches correspond either to the same subdivision level, or their subdivision levels differ by one. Patches that are adjacent to a patch from the next subdivision level are called *transition patches* (TPs). It is additionally required that TPs are always regular. This constraint is enforced during the subdivision preprocess by marking for subdivision all irregular patches that might become TPs. This constraint significantly simplifies the algorithm at the expense of only a small number of additional patches.

To obtain crack-free renderings, the hardware tessellator must evaluate adjacent patches at corresponding domain locations along shared boundaries. Setting the tessellation factors of shared edges to the same value will ensure this. However, TPs share edges with neighboring patches at a different subdivision level by definition. One solution to this problem would be using compatible power-of-two tessellation factors so that the tessellations will line up. However, allowing only power-of-two tessellation factors is a severe limitation that reduces the available flexibility provided by the tessellation unit. In order to avoid this limitation, each TP is split into several sub-patches using a case analysis of the arrangement of the adjacent patches. Since each patch boundary can either belong to the current or to the next subdivision level, there are only 5 distinct cases, as shown in Figure 9.

Each sub-domain corresponds to a logically separate subpatch, though each shares the same bi-cubic control points with its TP siblings. Evaluating a sub-patch involves a linear remapping of canonical patch coordinates (e.g., a triangular barycentric) to the corresponding TP sub-domain, followed by a tensor product evaluation of the patch. This means that each sub-domain type will be handled by draw calls requiring different constant hull and domain shaders, though these are batched according to sub-patch type. However, since the control points within a TP are shared for all sub-patches, the vertex and index buffers are the same. The overhead of multiple draw calls with different shaders but the same buffers becomes negligible for a larger number of patches.

By rendering TPs as several logically separate patches, all T-junctions in the patches are eliminated from the structure of a surface. This means that as long as consistent tessellation factors are assigned to shared edges, in principle a crack-free rendered surface is obtained. In practice however, due to the behavior of floating point numerics, additional care is required as discussed previously.

3.7.4. Optimizing Semi-Sharp Creases

Excluding crease edges, the time and space requirements of this feature-adaptive subdivision approach is linear in the number of extraordinary vertices in a mesh. Including crease edge, the time and space requirements are exponential, al-

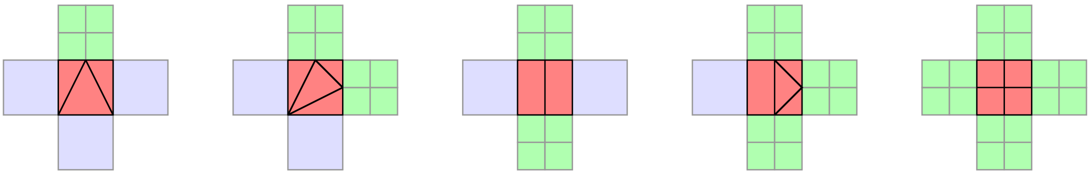

Figure 9: *There are five possible constellations for Transition Patches (TPs). While TPs are colored red, the current level of subdivision is colored blue and the next level is green. The domain split of a TP into several sub-patches allows full tessellation control on all edges, since shared edges always have the same length.*

though this growth is less than näive subdivision. To improve this behavior, Nießner et al. [NLG12] create optimized shaders specifically for handling semi-sharp creases. They consider only patches with isolated constant sharpness tags, which will appear after each subdivision level. Within such a patch, the unit square domain can be partitioned into 2 (integer sharpness) or 3 (fractional sharpness) zones, which can be directly evaluated using an eigen analysis of corresponding polynomial structures. This allows to immediately tessellated large patches with only a single crease tag, thus greatly improving the time and space requires of feature-adaptive subdivision.

3.7.5. Dynamic Feature-Adaptive Subdivision

An extension to the feature-adaptive subdivision algorithm has been proposed by Schäfer et al. [SRK*15]. The core idea is to enable an independent subdivision depth for every irregularity; i.e., locally-adaptive subdivision within a single mesh where the subdivision depth at a vertex is uncorrelated to those of other vertices. To this end, subdivision kernels fill a dynamic patch buffer on-the-fly with the appropriate number of patches corresponding to the chosen level-of-detail scheme. Especially in the context of large meshes, this reduces the number of generated and processed patches, thus improving the rendering performance. In the end, this provides an abstraction over patch regularities; i.e., a tess factor can be assigned to any patch of the base mesh irrespective of whether it is irregular or not.

3.8. Summary

Table 1 shows a comparison overview of different subdivision surface rendering methods, including approximate and accurate patching schemes. We report properties such as speed, accuracy and continuity, bit-wise exactness, and the flexibility of handling special features. Feature-adaptive subdivision is most flexible while achieving high frame rates. It can be also easily applied to other subdivision schemes such as Loop [Loo87], as shown by Huang et al. [HFN*14].

4. Adaptive Tessellation

In Section 3.6, we presented different methods for representing a subdivision surface so that it can be efficiently processed by tessellation hardware, which can require careful handling in the presence of extraordinary vertices or creases. However, even for an ordinary Catmull-Clark patch where analytic evaluation is straightforward, different tradeoffs must be made when the idealized surface is tessellated down to a discrete set of triangles. If the tessellation is too coarse (large triangles), the surface will be *under-tessellated*, leading to interpolation artifacts, faceting on silhouettes, and an undersampled displacement field. If the tessellation is too fine (small triangles), the surface will be *over-tessellated*, reducing rasterization efficiency. Modern GPUs (circa 2014) are still not optimized for pixel-sized triangles, which can make this performance cost significant. The desired tessellation threshold depends on the current viewpoint the surface is being rendered from, the material properties of the surface, and the performance demands of the underlying application. For example, surfaces with fine-scale displacement detail will require dramatically more tessellation than smooth, non-displaced geometry.

4.1. Heuristic Tessellation Strategies

The underlying tessellation hardware on current GPUs is visualized in Figure 3, requiring tessellation factors to be defined for each patch edge [Mor01]. A simple approach to computing tessellation factors is as a function of the distance from the eyepoint to the midpoint of a patch edge [NLMD12]. Another option is to fit a sphere around an edge and determine the tessellation factors from the projected spheres diameter in screen space [Can11]. Both methods are easy to compute and give the same result for a shared edge regardless of which patch is being considered, although edge length projection is not rotation-invariant (see Figure 10). Note that it is critical that tess factors for shared edges match in order to guarantee a crack-free rendering. Further heuristics are shown in the context of displacement mapping [NL13].

4.2. Pixel-Accurate Rendering

The concept of pixel-accurate rendering [YBP12, YBP14] is used to determine a tessellation factor that guarantees a tessellation of a surface differs from the true surface, when measured in screen-space pixel coordinates, by at most

	speed	exact limit surface	order of continuity	bitwise-exact edge		meshes with boundary	semi-sharp creases
				position	normal		
Stam	●○○	✓	C^2	–	–	–	–
PN-triangles	●●○	–	C^0	✓	–	✓	–
ACC-1	●●○	–	C^0	✓	–	✓	–
ACC-2	●●●	–	C^1	✓	–	✓	–
Feature-adaptive	●●●	✓	C^2	✓	✓	✓	✓

Table 1: *A comparison of properties of different subdivision surface rendering methods using hardware tessellation.*

half a pixel. For non-displaced Catmull-Clark surfaces, this is accomplished using a bounding structure called a *slefe*, meaning Subdividable Linear Efficient Function Enclosures [LP01]. These are piecewise linear upper and lower bounding polylines that can be computed using a precomputed table of numbers and a curve's Bézier control points. This notion is extended to surfaces using *slefe boxes*, whose projections can be used to estimate a tessellation factor for an entire patch. Since the tessellation factors for neighboring patches will likely differ on a shared edge between patches, the edge's tessellation factor is set to the larger tessellation factor estimated for the two incident patches.

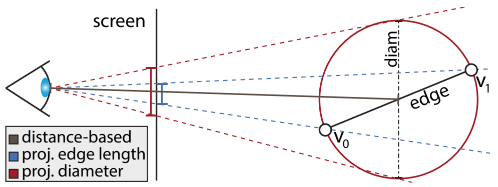

Figure 10: *Tessellation heuristics: in contrast to edge length projection (blue) the heuristic using an edges projected bounding sphere diameter is rotation invariant (red).*

4.3. Splitting Patches

For a large patch, there may not exist a set of edge tessellation factors that yields a good tessellation. This can occur for two reasons: the patch may have geometric or displacement detail that requires greater than the maximum edge tessellation factor (64 vertices per edge for most hardware), or the patch may have non-uniform geometric complexity on its interior that cannot be achieved just with edge constraints. In offline rendering systems, one approach that is used to overcome this problem is to split such patches into sub-domains, which can then either be processed by the tessellator or recursively split [CCC87]. Care must be taken to ensure that the resulting sub-patches align at edge boundaries to avoid severe surface cracking artifacts. One approach to achieve this alignment is to enforce consistent power-of-two constraints on all edges and then introduce stitching triangles between different splitting levels, but this approach is difficult to parallelize and prevents the resulting tessellation from adapting well to the underlying geometry.

To overcome the power-of-two constraint, *DiagSplit* allows crack-free patch splitting with arbitrary integer edge tessellation factors by performing splits along non-isoparametric lines in the *uv* parameter space [FFB*09]. DiagSplit evaluates a tessellation factor for each edge using one of the above methods, or determines that the edge is non-uniform and forces both patches incident on this edge to split. When all of a patch's incident edges have fixed tessellation factors it is sent to the hardware tessellator. The *FracSplit* algorithm improves upon DiagSplit to enable continuous level-of-detail [LPD14]. Unlike DiagSplit, FracSplit is able to handle fractional edge tessellation factors by smoothly interpolating the split from patch corners to the edge midpoint. This avoids visual popping during animation and camera motion while preserving a crack-free tessellation. Figure 11 shows a comparison of split patterns between *DiagSplit* and *FracSplit*.

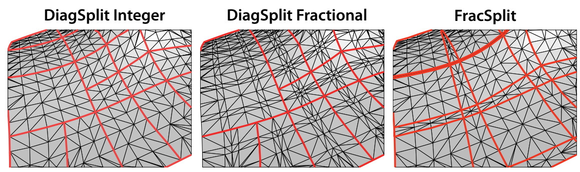

Figure 11: *DiagSplit and FracSplit patch-splitting and tessellation behavior. DiagSplit splits along a parametric line close to the middle of the patch, while FracSplit smoothly interpolates the parametric split between one corner of the patch and the edge midpoint.*

5. Displacement Mapping

In 1978, Blinn proposed perturbing surface normals using a wrinkle function [Bli78]. While this mimics the shading of a high-resolution surface, the geometry itself remains unchanged. This led Cook [Coo84] to develop *displacement mapping* to give objects more realistic silhouettes. Displacement mapping has since been used as a means to efficiently represent and animate 3D objects with high-frequency surface detail [SKU08]. Where texture mapping assigns color to surface points, displacement mapping assigns offsets, which are either scalar- or vector-valued. The advantages of displacement mapping are two-fold. First, only the vertices of a coarse base mesh need to be updated to animate the model. Second, since only the connectivity for the coarse mesh is needed, less space is required to store the equivalent, highly detailed mesh. In the following, we primarily consider scalar-valued displacements since they are faster to render and take up less storage. The displacement is then achieved by tessellating the base mesh and moving the generated vertices along their normal according to the value stored in the displacement map (see Figure 1).

Hardware tessellation is ideally suited for displacement mapping. A coarse mesh provides a base surface that is tessellated on-chip to form a dense triangle mesh that is immediately rasterized without further memory I/O. While conceptually simple and highly efficient, there are two major sources for artifacts that have to be addressed.

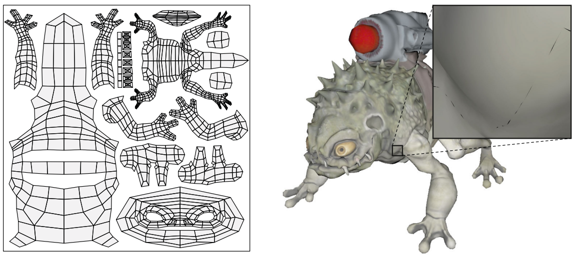

Figure 12: *Cracks on the displacement-mapped Monsterfrog (right) appear at uv chart boundaries (atlas left) when sampled displacement and normal values do not exactly match on both sides of a seam.*

First, before a displacement map can be applied, the base mesh is typically endowed with an explicit parameterization, often in the form of a 2D texture atlas (see [FH05] for a survey). Conceptually, seams must be introduced on edges to unfold the surface into the plane, creating a mapping from the plane to the surface. Points on seams map to more than one point in texture space, resulting in inconsistent values; bilinear texture filtering exacerbates this problem. For displacement mapping, these discontinuities in surface offset or normal can lead to unacceptable cracks in a rendered surface as shown in Figure 12.

Second, hardware tessellation is based on the dynamic retessellation of patches, so the underlying sampling pattern is continuously updated to achieve triangles of uniform size (see Section 4). However, continuously changing the sampling pattern creates swimming artifacts – the surface appears to fluctuate and the sampling pattern becomes visible. This effect is caused by under-sampling the displacement map while changing the sampling positions over time.

Avoiding these artifacts is an active research area. In the following we discuss displacement mapping methods and provide details on selected recent publications. Hiding seams in displacement mapping mainly depends on the underlying parameterization. Therefore, the approaches can be categorized into the following classes:

- *Texture Atlases 5.1:* The general case of explicitly parameterized meshes, as described above. The atlas can consist of multiple unconnected regions (charts).
- *Heightmaps 5.2:* Typically used for planar surface displacement using a texture atlas consisting of only a single, rectangular chart without seams.
- *Procedural Displacement 5.3:* Avoid texture related problems by amplifying geometry computationally.
- *Per-Face Texturing 5.4:* Methods where each patch maps to a unique texture tile with displacement values.

5.1. Texture Atlases

Providing consistent transitions between chart boundaries in a texture atlas is challenging [SWG*03] and leads to a wide range of approaches. Artifacts can be reduced by optimizing seam positions [SH02, LPRM02] or by creating textures with matching colors across seams [LH06]. However, minor discontinuities will always remain as long as chart boundaries differ in length or orientation in the texture domain. Small discontinuities are acceptable for color textures; however, for displacement textures they result in cracks and can be pronounced. Thus, parameterizations were proposed with consistent chart boundaries and orientation to obtain a perfect alignment of texel grids. Carr et al. [CHCH06, CH04] and [PCK04] employ quad segmentation on the input mesh and map the resulting charts to axis-aligned squares in the texture domain. This mapping induces distortions unless all quads in the segmentation are of equal size. Ray et al. [RNLL10] solve this issue by aligning matching boundary edges with an indirection map containing scaling and lookup information.

A different class of approaches aim to create watertight surfaces without modifying the parameterization. For instance, Sander et al. [SWG*03] close gaps after displacement by moving boundary vertices to a common, precomputed *zippering* path. González and Patow [GP09] insert a ribbon of triangles between charts in the texture domain to interpolate boundaries in a specialized shader program.

Texture coordinates are typically stored and processed as floating point values. Unfortunately, precision is unevenly distributed (see Goldberg [Gol91]); i.e., precision decreases with distance from the origin. This results in different sample positions, and thus displacement discontinuities, when interpolating texture coordinates on seam edges in different locations in the atlas, even if the edges' lengths are equal and consistently oriented. Castaño [Cas08] avoids these precision problems by pre-selecting one of the matching edges or vertices for sampling the seam. The texture coordinates of the preselection are stored for every patch vertex and edge, resulting in a consistent evaluation during rendering. Thereby, this approach is independent from boundary orientations at the cost of storing additional texture coordinates (16 for quads, 12 for triangles).

The majority of parameterization methods used for color texturing minimize only geometric metrics and assumes no prior knowledge of the signal to be stored. However, when the data to be stored is known (e.g., surface samples with distances for displacement mapping), this prior knowledge can well be used to optimize the parameterization, and to allocate more texels in regions with high detail. This inspired Sloan et al. [SWB98] and Sander et al. [SGSH02] to optimize the parameterization based on an importance measurement; e.g., the size of a triangle in the detailed mesh or the reconstruction error introduced. Following these approaches, Jang and Han [JH13, JH12] displace vertices generated with hardware tessellation into regions with high detail.

5.2. Heightfields

In applications such as digital elevation modeling and terrain rendering the underlying base model is typically spherical or locally planar. For example, a planet can be subdivided into mostly rectangular regions, which are then mapped to a square in the texture domain.

When using such *heightfields*, various problems arise. First, the amount of available elevation information typically does not fit into the GPU memory for rendering (e.g., the Earth's surface at a resolution of one texel per $1m^2$ would require 1.855 TB of memory). This problem can be solved by creating a hierarchy of different resolutions and only keeping a few levels in GPU memory at a time, as proposed by Tanner et al. [TMJ98]. Second, for watertight rendering, seams between heightfields, possibly at different resolutions, need to be handled. Third, the surface geometry should ideally be sufficiently dense to reconstruct details close to the observer and coarser at distance to allow for interactive rendering. For watertight rendering, this requires handling of patch boundaries with different mesh resolutions in addition to seams between heightfields. This led to a wide range of tessellation and level-of-detail schemes; see [PG07] for a survey.

Interactively rendering high-density heightfields requires displacing a densely tessellated mesh. Hardware tessellation is ideally suited for this task. Massive amounts of geometry can be adaptively generated from a coarse mesh, saving precious GPU memory, which in turn, allows for using higher resolution heightfields, since a large portion of the mesh to be displaced is generated on the fly.

Tatarchuk et al. [TBB10] subdivide the planar input geometry into equally sized sub-patches to overcome hardware-imposed tessellation density limitations. Instead of a uniform subdivision, Cantlay [Can11] subdivides the input geometry using a chunked-LOD approach [Ulr02] to allow higher tessellation close to the observer. During construction Cantlay restricts the patches to a power-of-two in relative size, which is then stored with each patch. Watertight rendering is achieved by making adjacent edges concur on a matching tessellation factor depending on the relative patch sizes (see Section 4.1).

In contrast to the previous methods, Bonaventura [Bon11] considers different heightmap resolutions (mipmaps) during rendering. The input mesh is subdivided into equally sized quads, and tessellation factors at edges are restricted to powers-of-two. The mipmaps for trilinear sampling are selected such that the average vertex density matches the texel density. Yusov and Shevtsov [YS11] compress heightfields in a GPU-friendly format that can be used to reduce memory I/O for out-of-core rendering of large data sets.

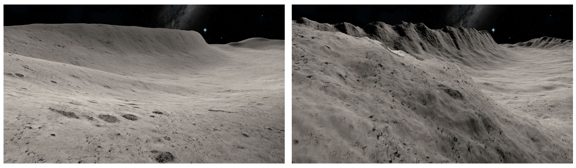

Figure 13: *Terrain rendering with a low-resolution heightfield (left) and procedurally amplifying geometry with high-frequency detail (right).*

5.3. Procedural Displacement

Modeling realistic environments such as cities or natural-looking plants is a time consuming process. Man-made structures and plants are often composed of simple shapes with small variations (e.g., plants with different numbers of leaves and variations in shape). Procedural approaches aim at creating massive content computationally. Applications include modeling cities, large realistic terrains, complex plants, or extremely small surface details (e.g., skin). Procedural methods offer a large variety of uses: content can be automatically generated, parameterized, stored and combined with artist-created content. On-the-fly generation enables rendering massive amounts of content with small I/O requirements with only a small set of parameters having to be uploaded. Therefore, it is reasonable to combine procedural techniques with hardware tessellation.

Bonaventura [Bon11] shows how to apply hardware tessellation to ocean rendering. Here, the ocean is represented by a procedural heightmap function defined over a ground plane. In the context of planar surface displacements Cantaly [Can11] shows how to amplify a terrain, which follows a base heightmap, with procedurally generated detail displacements as shown in Figure 13.

Instead of directly evaluating procedural heightmaps, geometry and scene properties can also be generated by a set of rules, affording potentially more complex kinds of content. This approach was first proposed by Lindenmayer [Lin68] for describing and researching plant growth. Each species is described by a *shape grammar* [Sti80] and individuals by a small set of parameters. Large amounts of plants are then obtained by interpreting the grammar for each individual. Shape grammars found widespread use in architectural modeling, city planning, simulation and content creation for movie production and games (see [WMWF07] for a survey).

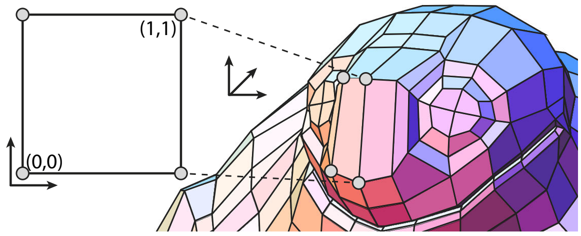

Figure 14: *Face-local texturing approaches implicitly parameterize of each face by the local vertex order.*

Marvie et al. [MBG*12] propose a method for evaluating shape grammars directly within the tessellation shaders. After grammar evaluation, a set of terminal symbols remain that are replaced by detailed geometry instances or simple textured quads (e.g., facade walls) in a geometry shader. For LOD rendering they switch between geometry and texture terminal symbols depending on the viewer distance. Experimental results show a massive city scene with about 100k buildings and 550k trees rendered at interactive rates on an Nvidia GTX 480, with buildings and trees generated from 2 and 7 different grammars. Grammars and parameters are adjustable, allowing for interactive feedback and verification. An explicit polygonal representation of the scene with detailed geometry would require 2.3 TB of GPU memory in contrast to 900 MB with the method of Marvie et al., mostly occupied by geometry terminal symbols.

5.4. Per-Face Texturing Methods

Most automatic global parameterization approaches either aim at creating as few seams, and thus charts, as possible or striving towards minimizing distortions resulting in more distinct charts. When packed into a texture atlas, charts must not overlap and are typically enclosed by a texel margin to prevent sampling from neighboring charts. This results in many texels not covered by charts and, thus, in an ineffective utilization of the available texture space. The use of mipmapping [Wil83] to prevent undersampling artifacts exacerbates the problem, requiring larger margins such that charts in lower resolution textures do not overlap. Maruya [Mar95] proposes to increase coverage by tightly packing triangles in arbitrary order into equally sized blocks. Therefore, each mesh triangle is mapped to a isosceles right triangle with edges being power-of-two fractions of the block size. Carr et al. [CH02] improve this approach by mapping adjacent triangles to blocks. This reduces discontinuities and enables mipmapping individual blocks.

Instead of a global parameterization, Burley and Lacewell [BL08] propose per-face texturing with each quad face implicitly parameterized by the order of its corner vertices (see Figure 14). Each face is assigned a power-of-two sized texture block enabling mipmapping each face individually. The full resolution and down-sampled face blocks are then packed into a global texture atlas. Further, indices to adjacent face blocks are stored with each face to enable seamless evaluation by sampling neighboring face textures at boundaries in their offline renderer. While this approach works well for offline rendering, evaluating and sampling neighboring faces through an indirection pointer introduces dependent texture reads which negatively impact the performance when applied on the GPU.

5.4.1. Multiresolution Attributes

Schäfer et al. [SPM*12] present a method to avoid texture-related artifacts by extending the concept of vertex attributes to the volatile vertices generated by hardware tessellation. To this end, they use a data structure that follows the hardware tessellation pattern, where for each generated vertex a set of attributes such as surface offset, normal or color is stored. This direct vertex-to-attribute mapping enables them to overcome under-sampling artifacts appearing when sampling attributes from textures.

Conceptually, their data structure is similar to the per-face texture tiles [BL08]. However, they store a linear array of attributes corresponding to hardware generated vertices for each face (see Figure 15). Providing consistent transitions between faces in tile-based texturing approaches is of paramount importance for preventing discontinuities and cracks. Hence, Schäfer et al. separately store attributes of inner face vertices from those at corners and edges shared between multiple faces. Attributes shared by adjacent faces are only stored once, resulting in a consistent evaluation and transitions between faces. This eliminates all discontinuities besides from those already present in the input mesh. During rendering, they use the implicit uv-coordinate of a patch in the domain shader to access the data in the linear array. In addition, they show filtering operations on the data and signal-adaptive storage of the data at multiple resolutions. The data structure further enables continuous level-of-detail without popping artifacts when using adaptive tessellation.

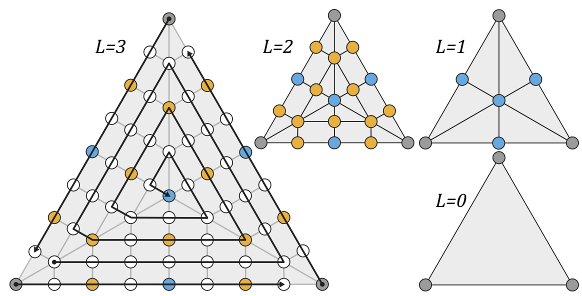

Figure 15: *Linearization of triangle tessellation pattern in inward-spiraling order (left). Vertex locations on different power-of-two tessellation patterns are present in higher levels at exact same uvw positions (vertices colored by level of first appearance).*

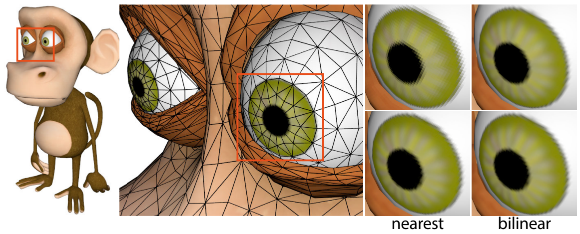

Figure 16: *Comparing the quality for color data; from left: rendering; close-up showing base geometry; close-up of the eye using uv-texturing (top) and the method of Schäfer et al. (bottom) showing nearest neighbor and bilinear filtering.*

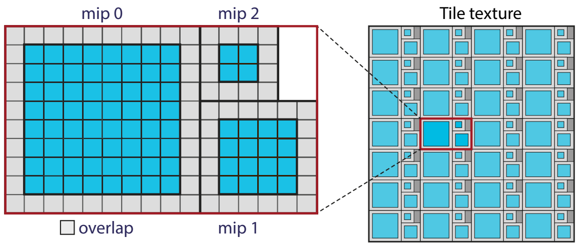

Figure 17: *Snippet of the tile-based texture [NL13] format used for displacement data (8×8 per tile; blue) showing a closeup of a single tile (red outline) including overlap region (gray) and mip levels.*

Comparison to UV-Textures The method of Schäfer et al. [SPM*12] and uv-textures are similar in terms of quality when using bi- and tri-linear filtering. However, Schäfer et al. avoid undersampling artifacts and cracks. Differences are visible when comparing nearest neighbor sampling which makes the underlying storage pattern (rectangular shape of texel for uv-textures, triangular pattern using their representation) visible (see Figure 16). Performance measurements show that their method is on-par with uv-textures.

5.4.2. Analytic Displacement Mapping

A major drawback to uv-texture displacement maps is the requirement for an additional map to retrieve normal information. This causes a significant amount of memory overhead and updating displacement data inconvenient since normals need to be re-computed with every surface update.

Nießner and Loop [NL13] present an approach that eliminates this problem by obtaining normal information directly from an *analytic* offset function. Their method appeared in the context of displaced subdivision surfaces, and formulates the displaced surface as

$$f(u,v) = s(u,v) + N_s(u,v)D(u,v), \tag{6}$$

where $s(u,v)$ is a base Catmull-Clark limit surface defined by a coarse base mesh, $N_s(u,v)$ is its corresponding normal field, and $D(u,v)$ is a scalar-valued displacement function. The important property is that the base surface is consistently C^2, except at a limited number of extraordinary vertices where it is still C^1. $D(u,v)$ is then defined by constructing a scalar-valued bi-quadratic B-spline with a Doo-Sabin subdivision surface structure [DS78], which is C^1 with vanishing first derivatives at extraordinary vertices. Thus, the displaced surface $f(u,v)$ is also C^1, facilitating smooth surface normals that can be derived analytically without requiring an explicit normal map. While this reduces memory consumption and rendering time, it also allows for efficient dynamic surface edits.

Tile-Based Texture Format In order to avoid texture seam misalignments, which plague classic uv-atlas parameterization texture methods, Nießner and Loop [NL13] propose a tile-based texture format to store their displacement data. They store a bi-quadratic displacement function whose coefficients are stored in an axis-aligned fashion in parameter and texture space. This can be seen as an improved GPU version of Ptex [BL08]; however, adjacent tile pointers, which are impractical on the GPU, are absent. Instead, a one-texel overlap per tile is stored to enable filtering while matching displacements at tile boundaries. An example with two texture tiles is shown in Figure 17 where each tile corresponds to a quad face of the Catmull-Clark control mesh. Tile edges are required to be a power-of-two (plus overlap) in size, that is, for a $tileSize = 2^k$ (for integer $k \geq 1$), tile edge lengths are of the form $tileSize + 2$. Adjacent tiles do not need to be the same size.

Additional care must be taken with overlap computations at extraordinary vertices, where four tiles do not exactly meet. The idea is to make all tile corners that correspond to the same extraordinary vertex equal in value by averaging corner values. As a result, $\frac{\partial}{\partial u}D = \frac{\partial}{\partial v}D = 0$ at these tile corners. While this limitation is unfortunate from a modeling perspective, it is beneficial from a rendering perspective, as it is guaranteed that the displacement spline $D(u,v)$ will be C^1 across all tile boundaries (see [Rei97] for the proof).

The format also stores a full mipmap pyramid [Wil83] for each tile in order to avoid undersampling artifacts. Since displacement values are coefficients of a bi-quadratic surface, mip pyramids are computed based on quadratic B-wavelets [Ber04]. All tiles are then efficiently packed in a global texture with mip levels of individual tiles stored next to each other (cf. Figure 17). While this leaves some unused space, it provides efficient data access due to cache coherency. Additionally, the tile size and an offset to the tile location within the global texture is stored in a separate buffer for each quad face. Tile data is then indexed by the face/patch ID.

Surface Evaluation The key idea behind this approach is to consider a higher-order displacement function which facilitate analytically determining normals on the displaced surface. The base surface $s(u,v)$ is the limit surface of the Catmull-Clark subdivision defined by a two-manifold control mesh, possibly with mesh boundaries and can be effi-

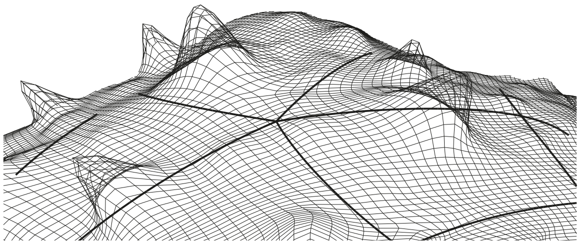

Figure 18: *Catmull-Clark base surface; patch boundaries shown as thick lines. Displacement surface: bi-quadratic Doo-Sabin B-splines; scalar coefficients on top of base surface normal field shown as thin lines.*

ciently evaluated and rendered using feature-adaptive subdivision [NLMD12]. A one-to-one correspondence between these quadrilateral faces and unit square domains of tiles is established, giving rise to a global parameterization of the surface (via a face ID; $u, v \in [1,0] \times [0,1]$ triple). The analytic displacement function $D(u,v)$ is defined by a scalar-valued bi-quadratic B-spline. These patches have an arrangement that is consistent with the Doo-Sabin [DS78] subdivision, meaning that the control mesh for the scalar displacement coefficients is *dual*, with refinements, to the control mesh of the base mesh. Note, that $D(u,v)$ is scalar-valued and can be thought of as a *height field*. In other words, both the base surface $s(u,v)$ and the displacement function $D(u,v)$ correspond to the same topological two-manifold, though embedded in $\mathbb{R}^3$ and $\mathbb{R}^1$, respectively. Figure 18 shows a detailed view of a model with base patch edges (thick curves) and the displacement function coefficients over the base surface (thin grid). For practicality's sake, a constraint is imposed at extraordinary vertices that causes first derivatives of the displacement function $D(u,v)$ to vanish at these points [Rei97]. This degeneracy implies that $D(u,v)$ is a globally C^1 function that can be evaluated over the entire manifold without particular case handling.

For given u, v coordinates and face ID, the displaced surface $f(u,v)$ of a patch can then be computed by evaluating the base patch $s(u,v)$, its normal $N_s(u,v)$, and the corresponding displacement function $D(u,v)$. The scalar displacement function is evaluated by selecting the 3×3 array of coefficients $d_{i,j}$ for the bi-quadratic sub-patch of $D(u,v)$, corresponding to the u, v value within its tile domain. The patch parameters u, v are transformed into the sub-patch domain $(\hat{u}, \hat{v})$ using the linear transformation T, where $\hat{u} = T(u)$ and $\hat{v} = T(v)$. T is defined as:

$$T(u) = u \cdot tileSize - \lfloor u \cdot tileSize \rfloor + \tfrac{1}{2}, \tag{7}$$

The scalar displacement function

$$D(u,v) = \sum_{i=0}^{2} \sum_{j=0}^{2} B_i^2(T(u)) B_j^2(T(v)) d_{i,j} \tag{8}$$

is then evaluated, where $d_{i,j}$ are the selected displacement coefficients, and $B_i^2(u)$ are the quadratic B-spline basis functions. The base surface normal $N_s(u,v)$ is obtained from the partial derivatives of $s(u,v)$:

$$N_s(u,v) = \frac{\frac{\partial}{\partial u} s(u,v) \times \frac{\partial}{\partial v} s(u,v)}{\left\| \frac{\partial}{\partial u} s(u,v) \times \frac{\partial}{\partial v} s(u,v) \right\|_2}. \tag{9}$$

In order to obtain the normal of the displaced surface $f(u,v)$, its partial derivatives are computed:

$$\begin{aligned} \frac{\partial}{\partial u} f(u,v) = \frac{\partial}{\partial u} s(u,v) + \frac{\partial}{\partial u} N_s(u,v) D(u,v) \\ + N_s(u,v) \frac{\partial}{\partial u} D(u,v), \end{aligned} \tag{10}$$

$\frac{\partial}{\partial v} f(u,v)$ is similar. Note that the derivatives of the displacement function are a scaled version of sub-patch derivatives:

$$\frac{\partial}{\partial u} D(u,v) = tileSize \cdot \frac{\partial}{\partial \hat{u}} \hat{D}(\hat{u}, \hat{v}). \tag{11}$$

Further, $\frac{\partial}{\partial u} s(u,v)$ can be directly obtained from the base surface. To find the derivative of $N_s(u,v)$, the derivatives of the (unnormalized) normal $N_s^*(u,v)$ are found using the Weingarten equation [DC76] (E, F, G and e, f, g are the coefficients of the first and second fundamental form):

$$\frac{\partial}{\partial u} N_s^*(u,v) = \frac{\partial}{\partial u} s(u,v) \frac{fF - eG}{EG - F^2} + \frac{\partial}{\partial v} s(u,v) \frac{eF - fE}{EG - F^2}, \tag{12}$$

$\frac{\partial}{\partial v} N_s^*(u,v)$ is similar. From this, the derivative of the normalized normal is found:

$$\frac{\partial}{\partial u} N_s(u,v) = \frac{\frac{\partial}{\partial u} N_s^*(u,v) - N_s(u,v)\left(\frac{\partial}{\partial u} N_s^*(u,v) \cdot N_s(u,v)\right)}{\|N_s^*(u,v)\|_2}, \tag{13}$$

$\frac{\partial}{\partial v} N_s(u,v)$ is similar. Finally, $\frac{\partial}{\partial u} f(u,v)$ is computed (analogous to $\frac{\partial}{\partial v} f(u,v)$) and thus $N_f(u,v)$.

Further, Nießner and Loop propose an approximate variant omitting the Weingarten term following Blinn [Bli78]. This is much faster from a rendering perspective and provides similar shading quality for small displacements.

Rendering surfaces with analytic displacements can be trivially performed by employing the hardware tessellator. The base surface $s(u,v)$, its derivatives $\frac{\partial}{\partial u} s(u,v)$, $\frac{\partial}{\partial v} s(u,v)$ and the displacement function $D(u,v)$ are evaluated in the domain shader along with the derivatives of the normal $\frac{\partial}{\partial u} N_s(u,v)$, $\frac{\partial}{\partial v} N_s(u,v)$. These computations are used in order to determine the vertices of the triangle mesh that are generated by the tessellator. The vertex attributes computed in the domain shader are then interpolated by hardware and available in the pixel shader where the derivatives of the displacement function $\frac{\partial}{\partial u} D(u,v)$ $\frac{\partial}{\partial v} D(u,v)$ are computed. This allows computing the derivatives of the displaced surface normal $\frac{\partial}{\partial u} f(u,v)$, $\frac{\partial}{\partial v} f(u,v)$ at each pixel independently providing per pixel surface normals for shading. Evaluating the surface normal $N_f(u,v)$ on a per-vertex basis would degrade rendering quality, due to interpolation artifacts.

	seamless	mipmapping	texture access	analytic normals	render performance	arbitrary meshes
UV-Atlas	–	limited	●●○	–	●●○	✓
UV-Atlas w. zippering [Cas08]	✓	limited	●○○	–	●○○	✓
Heightfields	✓	✓	●●●	✓	●●●	only planar
Multires. Attributes [SPM*13]	✓	✓	●●●	–	●●○	✓
Analytic Displacement [NL13]	✓	✓	●●●	✓	●●●	quad dominant

Table 2: *Comparison and properties of displacement mapping storage schemes (●●● is best): uv-Atlas parameterizations cannot fully hide displacement seams unless zippering is applied. Depending on the margin size between uv-boundaries only a few mip-levels are supported until charts overlap. Texture access indicates the storage and lookup requirements to fetch the data (e.g., one uv-coordinate per vertex for explicit parameterization vs. four uv-coordinates with zippering). Approaches providing low-cost seam handling or direct normal evaluation from displacement are superior in performance due to fewer texture fetches.*

5.5. Comparison of Texturing Methods

In Table 2, we compare texturing methods for storing and accessing displacement data to classical uv-atlases. While the zippering method allows using the existing textures to hide seams, the memory footprint and rendering performance is improved in the implicit parameterization schemes. Methods providing analytic normals are superior in performance although they are limited to planar and quad-dominant meshes.

5.6. Dynamic Displacement and Editing

Dynamic displacement and editing are important in digital content creation and for creating vivid virtual worlds in computer games. For procedural displacement dynamics are easily achieved by animating parameters, e.g., to create the water surface shown in Figure 19 in the Nvidia island example.

In the context of heightfields, Tatarchuk [Tat09] and Yusov [Yus12] realize deformations on terrains by blending between two maps or splatting a predefined decal to the heightfield texture. For multi-resolution heightfields this requires updating all mip-levels.

The situation is more difficult when uv-atlas textures are required, e.g., for models with a more complex topology in digital content creation. In this context, artists would like instant visual feedback during the design process while performing sculpting and painting operations. Adding detail to a model, e.g., wrinkles around the eye of a character, requires sufficient texture samples in this area. Where artists decide to add detail is unpredictable. This requires either the allocation of texture samples globally for all faces in advance

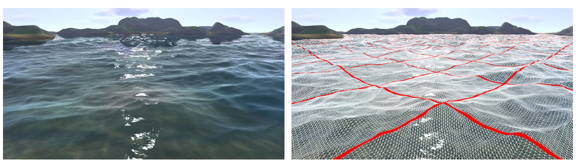

Figure 19: *Procedurally generated and animated water (left) and base patches (red outline) after tessellation (right).*

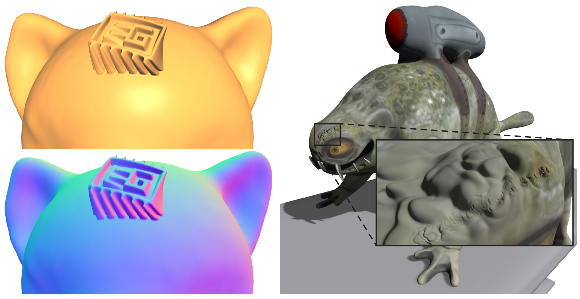

Figure 20: *Dynamic memory management for tile-based textures enables highly-detailed displacement sculpting on triangle meshes (with normal updates, left) and subdivision surfaces (right) in real-time.*

or performing texture resizing and re-sampling at run-time. Both approaches have severe disadvantages: first, the available memory and texture size on the GPU is limited. This restricts the number texture samples per face and thus the ability to add local detail. Second, resizing the texture on demand or allocating new face textures involves expensive memory I/O between host and device.

Dynamic GPU Memory Management To overcome this issue, Schäfer et al. [SKS13] propose a method for dynamic memory management for the per-face texturing methods in Section 5.4.1 and 5.4.2 that runs entirely on the GPU. The idea is to independently pre-allocate face blocks from mesh faces at different resolutions. At run-time these blocks are dynamically assigned to mesh faces for storing detail when editing the mesh. Providing a custom amount of face blocks for each resolution allows for using higher-detail textures on a subset of faces in contrast to global sample distribution. This makes the approach well-suited to applications that demand varying sample densities on different regions of a mesh. When more face blocks are requested than are available in the block pool, Schäfer et al. [SKNS14] either allocate and attach new sets of face blocks to the block pool or use a deallocation strategy in case the available GPU memory has been exhausted. First, for digital content creation face blocks can be downloaded and stored to disk. The face

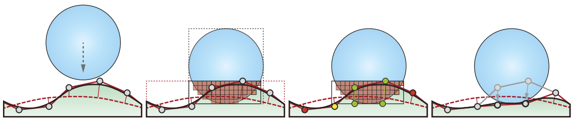

Figure 21: *Deformation algorithm overview: subdivision surfaces with quadratic B-Spline displacements are used as deformable object representation (left). The voxelization of the overlapping region is generated for an object penetrating the deformable surface (center left). The displacement control points are pushed out of the voxelization (center right), creating a surface capturing the impact (right).*

block is then replaced with a lower resolution version and finally deallocated by writing its block index back to the memory pool. Second, for gaming scenarios they propose decaying displacement over time, e.g., the imprint of a footstep, before the block is deallocated.

In their experimental results, they report the handling of local edits, including memory management and normal re-computation (needed for the multiresolution attributes scheme), in less than a millisecond, making this approach well-suited to real-time content creation tools and games. Figure 20 shows an example of the method for sculpting triangle and subdivision surface models with complex geometric detail.

Real-Time Surface Deformation on Object Collisions An essential aspect of dynamic scenes is the interaction between scene objects. However, due to tight time budgets many real-time applications support only rigid body collisions. In order to enable visual feedback when collisions cause scratches or other small surface deformations, materials like snow or sand are typically augmented with dynamically placed decal textures. However, decals are not able to modify the underlying surface geometry and therefore important visual cues such as occlusion or shadowing effects are missing.

Schäfer et al. [SKN*14] propose a real-time technique for automatically applying fine-scale surface deformations on object collisions. The core idea is to approximate geometric shapes with voxelizations, and apply deformations by dynamically updating displacement data. This is much more cost-efficient than a physically-correct soft body or finite element simulation, while providing visually plausible results. An overview of their technique is shown in Figure 21. During simulation they first apply a coarse rigid body simulation on the CPU to detect collision between deformable (e.g., a surface) and rigid objects. Deformable objects are represented by displaced subdivision surfaces. For colliding deformable-rigid object pairs they further process the deformation on the GPU by first generating a proxy geometry of the rigid object using a real-time binary voxelization as depicted in Figure 21 (center left). Then, they compute displacement offsets on the deformable surface to match the shape of the impact (Figure 21 center right and right). To this end, rays are cast from the deformable object's surface in order to determine displacement updates.

Figure 22: *Examples of real-time deformation method with fine-scale surface deformations on object collisions. The tracks of the car and barrels (left) are generated on-the-fly by updating the surface displacement map using a voxelization of the colliding objects as the user controls the car.*

Figure 22 shows an example of this deformation method with high surface detail, where a car is deforming a snowy surface. Processing times are between 0.1 and 0.2 ms per colliding object on an NVIDIA GTX 780, making this approach suitable for real-time applications with many colliding objects.

5.7. Displacement Acquisition

In order to recreate the shape of a detailed mesh from a tessellated coarse mesh, the differences between both meshes are sampled and stored in a displacement map. The following methods are used in practice: surface offsets can be computed by casting a ray from each texel's position on the coarse mesh in positive and negative normal direction and measuring the closest-hit distance with the detailed geometry. Unfortunately, the closest hit may not be the desired intersection point. In the case of the detail mesh being created from several subdivisions of the coarse mesh, each detail patch maps to a subspace of coarse mesh patches. This induces a direct mapping between both representations, enabling an easy transfer of detail to the displacement map.

Xia et al. [XGH*11] overcome these problems and restrictions by presenting a method for transferring detail from an arbitrary model to a semi-automatically created Catmull-Clark mesh based on polycubes [THCM04, HWFQ09]. Given a detailed input mesh M and a user-created coarse approximation P of the model consisting of equally sized cubes, the user defines correspondences by painting strokes on both meshes. A bijective map between both representations is found by computing a global distance field emerging from stroke endpoints. The distance field induces a triangulation on M and P. Therefore, positions inside each triangle are uniquely defined by distances to the triangle corners in M and P, resulting in a bijective map between both representations. With the polycube only consisting of square faces, a texture atlas is created containing all boundary faces, with faces between cubes omitted. Then, each chart in the texture atlas is populated by sampling positions in the detailed mesh using the distance field induced mapping between P and M. Finally, the polycube mesh is converted to a Catmull-Clark surface, that can then be rendered using methods outlined in Section 3. Although some user input is required, the repositioning of strokes on the polycubes enables control over distortions and assigned texture space of the resulting parameterization. The particular strength of this approach is the ability to compute a bijective map between two arbitrary meshes for transferring detail to a displacement map.

6. Patch Culling

On current hardware back-facing triangles are typically removed from the pipeline (culled) to avoid unnecessary rasterization and pixel shading. The application of back-face culling to geometry that is generated by GPU hardware tessellation is also straightforward. However, if the plane normals of all generated triangles for a given surface patch point away from the viewer, or patches are entirely occluded, considerable amounts of computation are still wasted for surface evaluation and triangle setup. In addition, view-frustum culling can be applied efficiently on a per patch level to further reduce patch tessellation and shading costs.

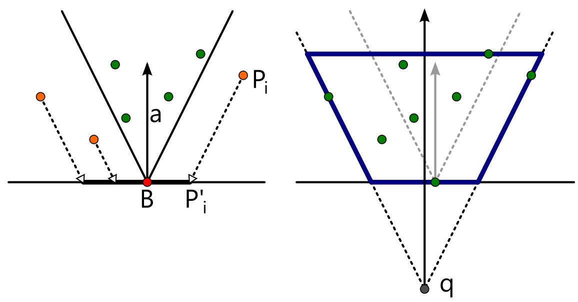

Figure 23: *Construction of an anchored truncated cone from the floating cone and the initial apex* **B***: control points outside the initial cone are projected onto the bottom plane, the apex of the truncated cone* **q** *is chosen such that the cone contains all control points.*

6.1. Back-patch Culling Techniques

6.1.1. Cone of Normals

Culling parametric patches can be achieved by computing a *cone of normals* for surface patches. A conservative bound of normals for a given parametric patch is defined by a cone axis **a**, a cone apex **L** and an aperture angle α.

Shirmun and Abi-Ezzi [SAE93] introduce such a technique for Bézier patches. They compute corresponding normal patches with the help of the analytic surface derivatives $N(u,v) = \partial B(u,v)/\partial u \times \partial B(u,v)/\partial v$. Hence, resulting normal patches are of degree $(3d_u - 1, 3d_v - 1)$ in the rational case, and of degree $(2d_u - 1, 2d_v - 1)$ in the polynomial case, where (d_u, d_v) are the degrees of the original patch. In the context of hardware tessellation, polynomial bi-cubic patches with $d_u = d_v = 3$ are commonly used.

Once the normal patch has been computed, the floating cone is constructed. It contains all normal directions of the original patch and is floating since it has no position, but rather only an orientation. The goal is to find the smallest enclosing sphere of a given set of (normalized) points in space. While there are exact, albeit computationally expensive, algorithms for its computation [Law65]), a practical solution is to exploit the convex hull property of Bézier patches and construct the corresponding bounding box (rather than a sphere) of the normal tip points $\mathbf{N}_i$. Therefore, a feasible guess for the cone axis **a** is

$$\mathbf{a} = \frac{1}{2}\begin{pmatrix} \max_i \mathbf{N}_{ix} - \min_i \mathbf{N}_{ix} \\ \max_i \mathbf{N}_{iy} - \min_i \mathbf{N}_{iy} \\ \max_i \mathbf{N}_{iz} - \min_i \mathbf{N}_{iz} \end{pmatrix}$$

with a corresponding aperture angle α given by $\cos(\alpha) = \min_i(\mathbf{a} \cdot \mathbf{n}_i)$ where $\mathbf{n}_i$ are the normals at patch control points. Note that the cone may be undefined if $\alpha > \pi/2$.

Once the floating cone is constructed, it has to be translated in order to contain the patch itself; i.e., include the patch control points. Such a cone is called an anchored truncated cone. First, a bottom control point **B** with respect to **a** is computed $\mathbf{B} = \mathbf{P}_i$, with i given by $\min_i(\mathbf{a} \cdot \mathbf{P}_i)$. An analogous point **T** on the top plane is also computed. Thus, the cone bottom plane is defined by $(\mathbf{B} - \mathbf{x}) \cdot \mathbf{a} = 0$. Second, every control point $\mathbf{P}_i$ is checked for enclosure in the translated cone. Points outside the cone are projected to the bottom plane. Projected points $\mathbf{P}'_i$ are then given by $\mathbf{BP}'_i = r(\mathbf{BP}_i - h\mathbf{a})$, with $h = \mathbf{BP}_i \cdot \mathbf{a}$, and $r = \left(\sqrt{\|\mathbf{BP}_i\|^2 - h^2} - h\tan(\alpha)\right) / \sqrt{\|\mathbf{BP}_i\|^2 - h^2}$. Upon applying this operation for all control points, the cone can be bounded on the bottom plane by the projected bounding box as shown in Figure 23. Finally, the top plane of the cone is determined analogously, which results in a bounding radius for both planes r_b (bottom plane) and r_t (top plane), and a center of gravity **c** of projected points on the bottom plane. The cone apex **q** of the cone containing all control points and normals is then given by $\mathbf{q} = \mathbf{c} - (r_b \cdot (\cos(\alpha)/\sin(\alpha))) \cdot \mathbf{a} + \mathbf{B}$. This provides the distance from the control points to the bottom and top plane $d_t = \mathbf{a} \cdot \mathbf{T} - \mathbf{a} \cdot \mathbf{q}$ and $d_b = \mathbf{a} \cdot \mathbf{B} - \mathbf{a} \cdot \mathbf{q}$. The distance z from the bottom plane to the front plane cone apex **L** is then given by $z = d_b \cdot \tan^2(\alpha)$, and leads directly to $\mathbf{L} = \mathbf{q} + \mathbf{a} \cdot (d_b - z)$. The distance to the top plane $y = d_t \cdot \tan^2(\alpha)$ and the back plane cone apex $\mathbf{F} = \mathbf{q} + \mathbf{a} \cdot (d_t - y)$ is provided accordingly (see Figure 24).

Given the cone of normals, culling for a given camera point **E** can be easily performed. First, normalized viewing directions are computed in respect to the cone apexes $\mathbf{V}_b = (\mathbf{E} - \mathbf{F})/\|\mathbf{E} - \mathbf{F}\|^2$ and $\mathbf{V}_t = (\mathbf{E} - \mathbf{L})/\|\mathbf{E} - \mathbf{L}\|^2$.

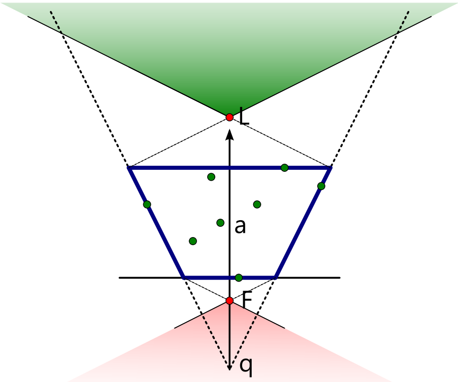

Figure 24: *Illustration of front facing (green) and back facing (red) regions of a cone's cross-section through its axis* **a**. *The apices of the back respectively front facing region are* **F** *and* **L**, *whereas* **q** *is the cone apex of the cone of normals.*

In the case where $\mathbf{a} \cdot \mathbf{V}_b \geq \sin(\alpha)$, the cone is back-facing and can thus be culled. Fully front-facing patches are identified if $\mathbf{a} \cdot \mathbf{V}_t \leq -\sin(\alpha)$. Otherwise, the patch is considered to be a silhouette containing front- as well as back-facing regions.

6.1.2. Approximate Cone of Normals

While the cone of normals technique provides relatively tight bounds, having to compute the normal patches is costly. Munkberg et al. [MHTAM10] propose an approximation of the cone of normals, which relies on a tangent and bi-tangent cone following Sederberg and Meyers [SM88].

The first step of their approach is to efficiently determine a cone axis **a**, which is simply approximated by the four patch corner points $\mathbf{a} = ((\mathbf{P}_{0n} - \mathbf{P}_{00}) + (\mathbf{P}_{nn} - \mathbf{P}_{n0})) \times ((\mathbf{P}_{n0} - \mathbf{P}_{00}) + (\mathbf{P}_{nn} - \mathbf{P}_{0n}))$. Note that the cone axis is also considered to be normalized. Next, aperture angles α_u and α_v of the tangent $\partial B(u,v)/\partial u$ and bi-tangent $\partial B(u,v)/\partial v$ patches, respectively, are derived by employing the convex hull property of the derivative Bézier patches. The angles of the tangent and bi-tangent cones are then combined in order to compute the cone angle α [SM88]:

$$\sin(\alpha) = \frac{\sqrt{\sin^2(\alpha_u) + 2\sin(\alpha_u)\sin(\alpha_v)\cos(\beta) + \sin^2(\alpha_v)}}{\sin(\beta)}, \tag{14}$$

where β is the smallest of the two angles between the u and v directions used to construct **a**. Given the cone axis **a** and the aperture α, patch culling is conducted the same way as described in Section 6.1.1.

6.1.3. Parametric Tangent Plane

Another way to perform patch culling is to consider the *parametric tangent plane* as proposed by Loop et al. [LNE11]. The parametric tangent plane $T(u,v)$ of a Bézier patch (also applicable to other polynomial patch types) $B(u,v)$ satisfies

$$\begin{bmatrix} B(u,v) \\ \frac{\partial}{\partial u}B(u,v) \\ \frac{\partial}{\partial v}B(u,v) \end{bmatrix} \cdot T(u,v) = \begin{bmatrix} 0 \\ 0 \\ 0 \end{bmatrix}.$$

Thus, $T(u,v)$ can be directly computed as

$$T(u,v) = \text{cross4}\left(B(u,v), \tfrac{\partial}{\partial u}B(u,v), \tfrac{\partial}{\partial v}B(u,v)\right), \tag{15}$$

where *cross4*() is the generalized cross product of 3 vectors in $\mathbb{R}^4$. For bi-cubic $B(u,v)$, the parametric tangent plane is a polynomial of bi-degree 7, written in Bézier form as

$$T(u,v) = \mathbf{B}^7(u) \cdot \begin{bmatrix} \mathbf{t}_{00} & \mathbf{t}_{01} & \cdots & \mathbf{t}_{06} & \mathbf{t}_{07} \\ \mathbf{t}_{08} & \mathbf{t}_{09} & \cdots & \mathbf{t}_{14} & \mathbf{t}_{15} \\ \vdots & \vdots & \ddots & \vdots & \vdots \\ \mathbf{t}_{48} & \mathbf{t}_{49} & \cdots & \mathbf{t}_{54} & \mathbf{t}_{55} \\ \mathbf{t}_{56} & \mathbf{t}_{57} & \cdots & \mathbf{t}_{62} & \mathbf{t}_{63} \end{bmatrix} \cdot \mathbf{B}^7(v),$$

where the $\mathbf{t}_i$ form an 8×8 array of control planes. Each $\mathbf{t}_i$ results from a weighted sum of *cross4*() products among the patch control points of $B(u,v)$. Note that $T(u,v)$, being of bi-degree 7, is one less in both parametric directions than expected from adding the polynomial degrees of inputs to the equation.

The next step is to employ the parametric tangent plane for visibility classification; i.e., determining whether a patch is front-facing, back-facing, or silhouette with respect to the eye point. The visibility for a patch $B(u,v)$ is classified by using its parametric tangent plane $T(u,v)$, $u,v \in [0,1]^2$, with respect to the homogeneous eye point **e** using the continuous visibility function:

$$\text{CVis}(B,\mathbf{e}) = \begin{cases} \text{back-facing}, & \text{if } (\mathbf{e} \cdot T(u,v) < 0), \\ \text{front-facing}, & \text{if } (\mathbf{e} \cdot T(u,v) > 0), \\ \text{silhouette}, & \text{otherwise.} \end{cases}$$

Computing $\text{CVis}(B,\mathbf{e})$ precisely will require costly iterative techniques to determine the roots of a bivariate polynomial. Instead, Loop et al. [LNE11] suggest a more practical discrete variant based on the Bézier convex hull of the scalar valued patch

$$\mathbf{e} \cdot T(u,v) = \mathbf{B}^7(u) \cdot \begin{bmatrix} \mathbf{e}\cdot\mathbf{t}_0 & \mathbf{e}\cdot\mathbf{t}_1 & \cdots & \mathbf{e}\cdot\mathbf{t}_6 & \mathbf{e}\cdot\mathbf{t}_7 \\ \mathbf{e}\cdot\mathbf{t}_8 & \mathbf{e}\cdot\mathbf{t}_9 & \cdots & \mathbf{e}\cdot\mathbf{t}_{14} & \mathbf{e}\cdot\mathbf{t}_{15} \\ \vdots & \vdots & \ddots & \vdots & \vdots \\ \mathbf{e}\cdot\mathbf{t}_{48} & \mathbf{e}\cdot\mathbf{t}_{49} & \cdots & \mathbf{e}\cdot\mathbf{t}_{54} & \mathbf{e}\cdot\mathbf{t}_{55} \\ \mathbf{e}\cdot\mathbf{t}_{56} & \mathbf{e}\cdot\mathbf{t}_{57} & \cdots & \mathbf{e}\cdot\mathbf{t}_{62} & \mathbf{e}\cdot\mathbf{t}_{63} \end{bmatrix} \cdot \mathbf{B}^7(v).$$

Patch visibility classification reduces to counting the number of negative values, N_{cnt}, produced by taking the 64 dot products $\mathbf{e} \cdot \mathbf{t}_i$ using the discrete visibility function:

$$\text{DVis}(B,\mathbf{e}) = \begin{cases} \text{back-facing}, & \text{if } (N_{cnt} = 64), \\ \text{front-facing}, & \text{if } (N_{cnt} = 0), \\ \text{silhouette}, & \text{otherwise.} \end{cases}$$

The classification produced by $\text{DVis}(B,\mathbf{e})$ is then a conservative approximation of $\text{CVis}(B,\mathbf{e})$. Therefore, it is possible

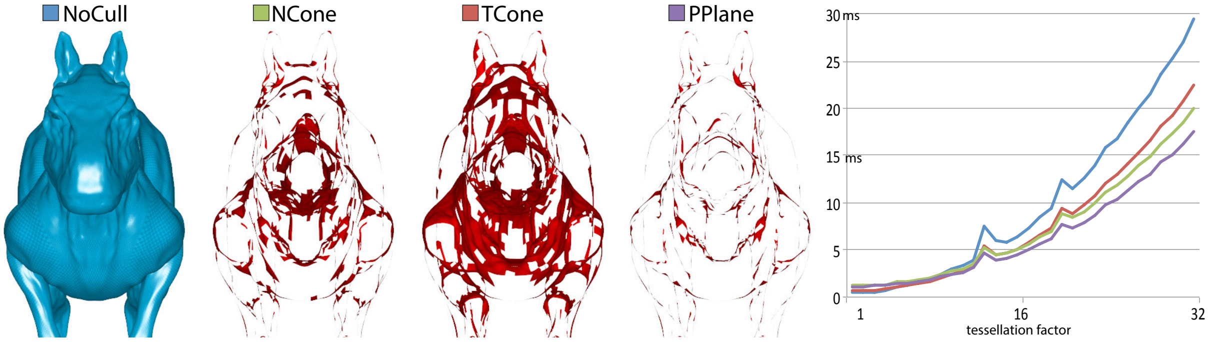

Figure 25: *Comparison of back-patch culling strategies applied to the* Killeroo *model shown left, which is composed of 11532 Bézier patches. For each comparison, wasted computations are visualized; i.e., areas processed by the tessellator with back-facing surface normals (less area is better). The cone of normals [SAE93] (NCone, 3697 patches culled) is effective, but costly for dynamic scenes. Its approximation from tangent and bi-tangent cones is faster to compute, but less precise [SM88] (TCone, only 2621 patches culled). Parametric tangent planes are faster than the cone of normals, and more effective [LNE11] (PPlane, 4604 patches culled). The comparison in rendering times in milliseconds is shown on the right for different tessellation factors.*

for DVis$(B, \mathbf{e})$ to classify a front- or back-facing patch as a silhouette in error. Loop et al. [LNE11] also provide an efficiently parallelized version to compute and evaluate the parametric tangent plane on the GPU.

6.1.4. Summary

Back-patch culling approaches are evaluated using the SimpleBezier example from the DirectX 11 SDK running on an NVIDIA GTX 480. It is most efficient to implement culling tests in a separate compute shader then feed the decision into the constant hull shader. The number of culled patches is determined for 10K random views to obtain a meaningful metric for the effectiveness of back-patch culling. Corresponding average cull rates for three popular models are listed in Table 3. Results are shown for the accurate cone of normals (NCONE), the approximate cone of normals (TCONE), and the parametric tangent plane (PPLANE) approach. PPLANE requires 0.76 ms per frame to cull 4604 patches. This is faster than NCONE, which needs 0.86 ms to cull 3697 patches. For tessellation factors larger than 8, the additional cull precision pays off, and PPLANE's time per frame is lower than TCONE, which needs 0.36 ms, but only culls 2621 patches. While TCONE provides the lowest culling rates, it is computationally the fastest. The computation costs and culling rates of NCONE are between TCONE and PPLANE. PPLANE performs the most accurate culling, and is the best method for highly-tessellated surfaces. Note that PPLANE does not provide a normal approximation as a side product, which is useful in some scenarios (e.g., for occlusion and view-frustum culling; cf. Section 6.2). In almost every scenario (i.e., tessellation factors greater than 4), back-patch culling comes out ahead, making it beneficial to many real-time applications. A visualization of culling results and corresponding frame render timings for a representative view is shown in Figure 25. In this example, all meshes are fully dynamic and skinned, thus vertices are updated every frame. In the case of rigid models, culling computations can be partly pre-calculated and cached. For instance, a normal cone can be pre-computed for every patch, leaving only a dot product evaluation at runtime for the culling test. An equivalent option for static models exists for PPLANE.

6.2. Patch-based Occlusion Culling

A general drawback to back-patch culling methods is the inability to address displaced patches. Hasselgren et al. [HMAM09] attempt to tackle this problem by introducing a Taylor expansion and applying interval arithmetic. This involves significant computational overhead and restricts dynamic tessellation densities. Nießner and Loop [NL12] introduce a culling method based on occlusion information to overcome this limitation.

Occlusion Culling Pipeline Patch-based occlusion culling works by maintaining visibility status bits (visible, occluded, or newly-visible) of individual patches as each frame is rendered. Assume that a frame has already been rendered and these status bits have been assigned to patches. At the beginning of a new frame, patches marked as visible are rendered. From the Z-buffer of this frame, a hierarchical Z-buffer (or

	Big Guy (3570)	Monster Frog (5168)	Killeroo (11532)
TCONE	1260 (35%)	1911 (37%)	3790 (33%)
NCONE	1601 (45%)	2286 (44%)	4685 (40%)
PPLANE	1729 (48%)	2478 (48%)	5206 (45%)

Table 3: *Average cull rates of different culling approaches: the accurate cone of normals [SAE93] (*NCONE*), the approximate cone of normals [SM88] (*TCONE*), and the parametric tangent plane [LNE11] (*PPLANE*).*

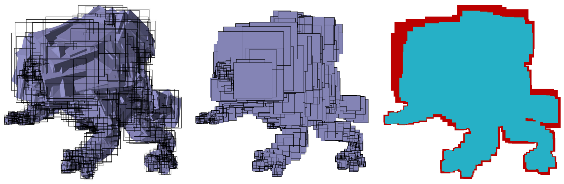

Figure 26: *Different bounding methods for displaced surfaces visualizing object (purple) and screen space (black quads) bounds: OBB (object-oriented bounding box [MHTAM10]), CAF (camera aligned frustum [NL12]) and a comparison between OBB (red) and CAF (blue); both using the same, approximate cone of normals.*

(a) 5.7 vs 12.1 ms (b) 3.4 vs 9.0 ms

Figure 27: *Patch-based occlusion culling [NL12] performed on per-patch basis: of patches with and without displacements. The images above are rendered with culling disabled and enabled; performance gains are below the respective image. (a)* 64.2% *patches culled, (b)* 70.6% *patches culled.*

Hi-Z map) [GKM93] is built using a compute shader (or CUDA kernel). Next, all patches are occlusion tested against the newly-constructed Hi-Z map. Patches passing this test (i.e., not occluded) are either marked as visible if they were previously visible, or newly-visible if they were previously occluded; otherwise they are marked as occluded. Finally, all patches marked as newly-visible and visible are rendered to complete the frame.

Computing Occlusion Data In order to obtain occlusion information, the depth buffer resulting from rendering the visible patches is used to generate a Hi-Z map [GKM93], [SBOT08]. The Hi-Z map construction is similar to standard mipmapping where four texels are combined to determine a single texel in the next mip level. Instead of averaging texels, the value of the new texel is set to the maximum depth of the corresponding four child texels. Thus, within a region covered by a particular texel (no matter which mip level) a conservative bound is given, such that no objects with larger distance to the observer are visible at the texel's location.

Occlusion Cull Decision Nießner and Loop [NL12] use bicubic Bézier patches as a representative patch primitive, but the approach could be applied to other patching schemes as well. In order to determine the visibility of a patch, its axis-aligned bounding box (AABB) is computed in clip space. The AABB's front plane is then tested against the Hi-Z map. Depending on the bounding box width and height in screen space, a particular level of the Hi-Z map is chosen: $level = \lceil \log_2(\max(width, height)) \rceil$. The bounding box area is conservatively covered by at most 4 texels of the selected Hi-Z map level. Considering multiple Hi-Z map entries allows for achieving better coverage.

Occlusion Culling of Displaced Patches Computation of occlusion information is the same for patches with and without displacements. One way to bound displaced patches is to extend patch OBBs with respect to patch displacements and corresponding patch normals [MHTAM10]. Tighter patch bounds are obtained when applying a camera-aligned frustum (CAF) [NL12]. A CAF is a frustum whose side planes contain the origin in camera space, which corresponds to the eye point in viewing space. Figure 26 shows the difference between OBB bounds [MHTAM10] and CAF bounds [NL12] using the same cone of normals to bound the displaced patches.

6.2.1. Summary

Similar to back-patch culling, computations for occlusion culling on current GPUs can be most efficiently obtained in a separate compute shader. Resulting culling decisions are then read by the hull shader, and patch tessellation factors are set to zero for culled patches.

Occlusion Culling within Individual Objects Since culling is performed on a per-patch basis, it can be applied to individual models and ignore occluded patches. In order to obtain meaningful culling rate measurements, average culling rates are determined using 1K different cameras views and models with and without displacement. Each view contains the entire object to prevent view frustum culling influencing the measurements.

Occlusion culling for non-displaced models is tested on the *Killeroo* and *Big Guy* model, achieving an average culling rate of 27.9% and 26.76%, respectively. In contrast, the best back-patch culling algorithm [LNE11] culls 38.7% and 37.8% of the patches. However, occlusion culling detects and culls significantly more patches with increased depth complexity since back-patch culling algorithms cannot take advantage of inter object/patch occlusions.

Occlusion culling for models with displacements is tested on the *Monster Frog* and the *Cow Carcass* model. Corresponding culling rates for different cull kernels are shown in Table 4. The camera-aligned frustum (CAF) is always more effective than the object-oriented bounding box (OBB) as it provides tighter space bounds. Both approaches involve the same computational cost.

General Occlusion Culling for Scenes Realistic applications involve scenes with multiple objects consisting of both

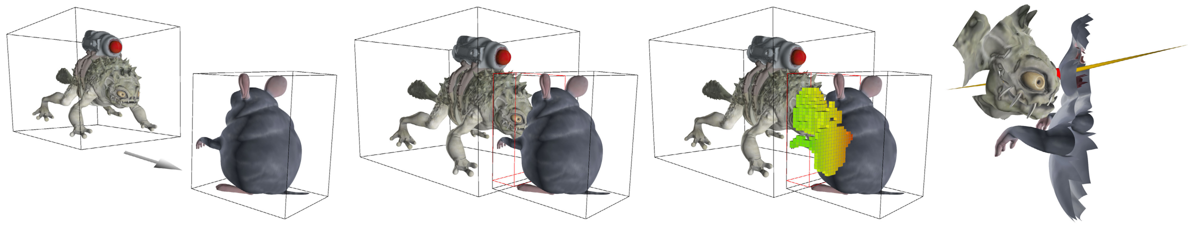

(a) (b) (c) (d)

Figure 28: *Visualizing collision detection for dynamically tessellated objects. The* Monster Frog *is moving towards the* Chinchilla *(a). At one point the OBBs of both objects intersect (b, red box) and the containing geometry is voxelized (c). This provides a collision point and corresponding surface normals (d). Patches shown in the last image could not be culled against the intersecting OBB and thus are potential collision candidates contributing to the voxelization.*

triangle and patch meshes. Two simple example scenes are shown in Figure 27 (the ACoN kernel is used for displaced models). In the first scene containing 27K patches a culling rate of 64.2% for the view shown in Figures 27(a) is achieved. Rendering is sped up by a factor of 2.1 (using a tessellation factor of 16). As expected, higher depth complexity results in more patches to be culled. Occlusion culling also benefits from triangle mesh occluders as shown in the second test scene (5.5K patches and 156 triangles). A culling rate of 70.6% is achieved for the view shown in Figure 27(b). As a result, render time is reduced by a factor of 2.6 (using a tessellation factor of 32).

	OBB		CAF	
	ACoN	CoN	ACoN	CoN
Frog	12.1%	14.0%	17.0%	18.4%
Frog^2	25.1%	26.4%	29.4%	30.9%
Cow	14.1%	15.6%	17.6%	18.7%
Cow^2	27.9%	29.1%	31.2%	32.7%

Table 4: *Average occlusion culling rates for displaced models; ^{2} denotes the respective model after one level of subdivision (i.e., four times more patches). While* OBB *performs occlusion culling using the bounds by [MHTAM10],* CAF *uses the camera-aligned frustum by [NL12].* ACoN *and* CoN *refer to the approximate and accurate cone of normal variant.*

Overall, patch-based occlusion culling significantly reduces tessellation and shading work load allowing for faster rendering. In contrast to back-patch culling approaches, the culling rate on single objects is slightly lower. However, occlusion culling is capable of handling displaced objects which are widely used in the context of hardware tessellation with increased effectiveness at higher depth complexities.

7. Collision Detection for Hardware Tessellation

Collision detection for hardware tessellation is particularly challenging since surface geometry is generated on-the-fly, based on dynamic tessellation factors and displacement values. Ideally, the same geometry used for rendering should be also taken into account to simulate physics. Nießner et al. [NSSL13] propose such an approach which provides collision results for dynamic objects directly on the GPU. The key idea is to detect collisions using voxelized approximations of hardware generated, possibly displaced and animated, detail geometry.

Collision Candidates The first step of the algorithm is to identify potential collision candidates. Therefore, object oriented bounding boxes (**OBBs**) are computed, and each object pair is tested for the corresponding OBB intersection. If there is no intersection, there can be no collision (early exit). Otherwise, a shared intersection volume between the two respective objects is defined. Next, a compute kernel is used to determine patches that are included in the shared volumes. In order to account for patch displacements, the cone of normals techniques, [SAE93] (accurate cone) or [SM88] (approximate cone), is used. Computing corresponding patch bounds is similar to patch-based occlusion culling [NL12].

Voxelization The core idea of the collision test is to voxelize the rendering geometry of the current frame. In this stage, only patches that were identified as collision candidates are considered in order to improve performance. These are all transformed into the space of the intersecting volume, which is used as a basis for a binary voxelization. Inside patches are then voxelized using a modified version of the practical algorithm by Schwarz [Sch12].

Collision Detection Collision detection is based on the binary voxelizations, which are obtained every frame for each non-zero shared volume of all object pairs. Given two solid voxelizations, embedded in a shared space, collisions are detected by pairwise voxel comparisons. Since voxel representations are binary, 32 voxel comparisons can be performed using a single bitwise AND-operation. In addition to collision positions, corresponding surface normals are obtained based on voxel neighborhoods, i.e., normals are derived by using the weighted average of the vectors between the current voxel and its 26 neighbors. This test may be extended by an additional pass to determine patch IDs and u, v coordinates of collision points.

Figure 28 shows how collision detection is applied to a simple test scene with two objects. Computational overhead is well below a millisecond.

8. Conclusion

In this survey, we provide an overview of state-of-the-art rendering techniques for hardware tessellation. By supporting programmable geometric amplification, the hardware tessellator enables real-time applications to efficiently render surfaces with very high geometric detail. We have covered ways to transform traditional surface representations so that they are amenable to the hardware tessellation pipeline. Many of these methods have already found application in industry; e.g., Pixar's *Open Subdiv* [Pix12], which is based on [NLMD12], is now part of various authoring tools such as Autodesk Maya. We believe future generations of video games and authoring tools will continue to benefit from the massively parallel hardware tessellation architecture.

Many of the ideas we have covered follow a common theme, where approaches that have proven successful in offline, production-quality rendering applications are adapted and re-purposed to the hardware tessellation pipeline. These ideas include exact handling of semi-sharp creases [Nie13], *DiagSplit* [FFB*09] and *FracSplit* [LPD14], both based on the Reyes split-dice pipeline, and tile-based displacement textures [NL13], which can be seen as a GPU analog of Ptex [BL08]. Moving forward, research in this area seeks to allow artists and developers to use the expensive techniques and representations present in content authoring tools and achieve fast, high-quality, and artifact-free renderings of this content in real-time applications.

We hope this survey will inspire future research in this exciting area. Hardware vendors are currently working on tessellation support in next-generation mobile graphics processors [Nvi13], [Qua13]. This will greatly widen the range of applications of the algorithms presented in this survey; given the power and memory constraints of mobile hardware, future research could include novel displacement storage and (de)compression schemes to reduce memory consumption, or tessellation algorithms with less computational overhead, e.g., refraining from fractional tessellation while still providing continuous level-of-detail rendering.

References

[AB06] ANDREWS J., BAKER N.: Xbox 360 System Architecture. *IEEE Micro 26*, 2 (2006), 25–37. 0

[BA08] BOUBEKEUR T., ALEXA M.: Phong Tessellation. *ACM Trans. Graph. 27*, 5 (2008), 141:1–141:5. 1

[Ber04] BERTRAM M.: Lifting Biorthogonal B-spline Wavelets. In *Geometric Modeling for Scientific Visualization*. Springer, 2004, pp. 153–169. 13

[BL08] BURLEY B., LACEWELL D.: Ptex: Per-Face Texture Mapping for Production Rendering. In *Proceedings of EGSR* (2008), pp. 1155–1164. 12, 13, 22

[Bli78] BLINN J. F.: Simulation of Wrinkled Surfaces. *Computer Graphics (Proceedings of SIGGRAPH) 12*, 3 (1978), 286–292. 9, 14

[Bon11] BONAVENTURA X.: Terrain and Ocean Rendering with Hardware Tessellation. In *GPU Pro 2*. A K Peters, 2011, pp. 3–14. 11

[BS02] BOLZ J., SCHRÖDER P.: Rapid evaluation of Catmull-Clark subdivision surfaces. In *Proceedings of the International Conference on 3D Web Technology* (2002), ACM, pp. 11–17. 4

[BS05] BOUBEKEUR T., SCHLICK C.: Generic Mesh Refinement on GPU. In *Proceedings of HWWS* (2005), ACM, pp. 99–104. 1

[BS08] BOUBEKEUR T., SCHLICK C.: A Flexible Kernel for Adaptive Mesh Refinement on GPU. *Computer Graphics Forum 27*, 1 (2008), 102–114. 1

[Can11] CANTLAY I.: DirectX 11 Terrain Tessellation. Nvidia whitepaper, 2011. 8, 11

[Cas08] CASTAÑO I.: Next-Generation Rendering of Subdivision Surfaces. Talk at SIGGRAPH 08, 2008. 10, 15

[CC78] CATMULL E., CLARK J.: Recursively Generated B-Spline Surfaces on Arbitrary Topology Meshes. *Computer-Aided Design 10*, 6 (1978), 350–355. 4

[CCC87] COOK R. L., CARPENTER L., CATMULL E.: The Reyes Image Rendering Architecture. *Computer Graphics (Proceedings of SIGGRAPH) 21*, 4 (1987), 95–102. 9

[CH02] CARR N. A., HART J. C.: Meshed Atlases for Real-Time Procedural Solid Texturing. *ACM Trans. Graph. 21*, 2 (2002), 106–131. 12

[CH04] CARR N. A., HART J. C.: Painting Detail. *ACM Trans. Graph. 23*, 3 (2004), 845–852. 10

[CHCH06] CARR N. A., HOBEROCK J., CRANE K., HART J. C.: Rectangular Multi-Chart Geometry Images. In *Proc. SGP'06* (2006), pp. 181–190. 10

[Coo84] COOK R.: Shade Trees. *Computer Graphics (Proceedings of SIGGRAPH) 18*, 3 (1984), 223–231. 9

[DC76] DO CARMO M.: *Differential Geometry of Curves and Surfaces*, vol. 1. Prentice-Hall, 1976. 14

[DKT98] DEROSE T., KASS M., TRUONG T.: Subdivision Surfaces in Character Animation. In *Proceedings of SIGGRAPH 98* (1998), Annual Conference Series, ACM, pp. 85–94. 4

[DS78] DOO D., SABIN M.: Behaviour of Recursive Division Surfaces near Extraordinary Points. *Computer-Aided Design 10*, 6 (1978), 356–360. 13, 14

[EML09] EISENACHER C., MEYER Q., LOOP C.: Real-Time View-Dependent Rendering of Parametric Surfaces. In *Proceedings of I3D'09* (2009), pp. 137–143. 1

[FFB*09] FISHER M., FATAHALIAN K., BOULOS S., AKELEY K., MARK W., HANRAHAN P.: DiagSplit: Parallel, Crack-Free, Adaptive Tessellation for Micropolygon Rendering. *ACM Trans. Graph 28*, 5 (2009), 150. 1, 9, 22

[FH05] FLOATER M. S., HORMANN K.: Surface Parameterization: A Tutorial and Survey. In *Advances in Multiresolution for Geometric Modelling*. Springer, 2005, pp. 157–186. 10

[GKM93] GREENE N., KASS M., MILLER G.: Hierarchical Z-Buffer Visibility. In *Proceedings of SIGGRAPH* (1993), Annual Conference Series, ACM, pp. 231–238. 20

[Gol91] GOLDBERG D.: What Every Computer Scientist Should Know About Floating-point Arithmetic. *ACM Comput. Surv. 23*, 1 (Mar. 1991), 5–48. 10

[GP09] GONZÁLEZ F., PATOW G.: Continuity Mapping for Multi-Chart Textures. *ACM Trans. Graph. 28* (2009), 109:1–109:8. 10

[Gre74] GREGORY J.: Smooth Interpolation without Twist Constraints. *Computer Aided Geometric Design* (1974), 71–87. 6

[HDD*94] HOPPE H., DEROSE T., DUCHAMP T., HALSTEAD M., JIN H., MCDONALD J., SCHWEITZER J., STUETZLE W.: Piecewise Smooth Surface Reconstruction. In *Proceedings of SIGGRAPH* (1994), ACM, pp. 295–302. 4

[HFN*14] HUANG Y.-C., FENG J.-Q., NIESSNER M., CUI Y.-M., YANG B.: Feature-Adaptive Rendering of Loop Subdivision Surfaces on Modern GPUs. *Journal of Computer Science and Technology 29*, 6 (2014), 1014–1025. 8

[HLS12] HE L., LOOP C., SCHAEFER S.: Improving the Parameterization of Approximate Subdivision Surfaces. *Computer Graphics Forum 31*, 7 (2012), 2127–2134. 6

[HMAM09] HASSELGREN J., MUNKBERG J., AKENINE-MÖLLER T.: Automatic Pre-Tessellation Culling. *ACM Trans. Graph. 28*, 2 (2009), 19. 19

[HWFQ09] HE Y., WANG H., FU C.-W., QIN H.: A Divide-and-Conquer Approach for Automatic Polycube Map Construction. *Computers & Graphics 33*, 3 (2009), 369–380. 16

[JH12] JANG H., HAN J.: Feature-Preserving Displacement Mapping with Graphics Processing Unit (GPU) Tessellation. *Computer Graphics Forum 31*, 6 (2012), 1880–1894. 11

[JH13] JANG H., HAN J.: GPU-optimized indirect scalar displacement mapping. *Computer-Aided Design 45*, 2 (2013), 517–522. 11

[KMDZ09] KOVACS D., MITCHELL J., DRONE S., ZORIN D.: Real-Time Creased Approximate Subdivision Surfaces. In *Proceedings of I3D'09* (2009), ACM, pp. 155–160. 6

[Law65] LAWSON C.: The Smallest Covering Cone or Sphere. *SIAM Review 7*, 3 (1965), 415–416. 17

[LH06] LEFEBVRE S., HOPPE H.: Appearance-Space Texture Synthesis. *ACM Trans. Graph. 25*, 3 (2006), 541–548. 10

[Lin68] LINDENMAYER A.: Mathematical Models for Cellular Interactions in Development I. Filaments with one-sided Inputs. *Journal of Theoretical Biology 18*, 3 (1968), 280–299. 11

[LNE11] LOOP C., NIESSNER M., EISENACHER C.: Effective Back-Patch Culling for Hardware Tessellation. *Proceedings of Vision, Modeling, and Visualization* (2011), 263–268. 18, 19, 20

[Loo87] LOOP C.: *Smooth Subdivision Surfaces Based On Triangles*. Master's thesis, University of Utah, 1987. 8

[LP01] LUTTERKORT D., PETERS J.: Optimized Refinable Enclosures of Multivariate Polynomial Pieces. *Computer Aided Geometric Design 18*, 9 (2001), 851–863. 9

[LPD14] LIKTOR G., PAN M., DACHSBACHER C.: Fractional Reyes-Style Adaptive Tessellation for Continuous Level of Detail. *Computer Graphics Forum 33*, 7 (2014), 191–198. 9, 22

[LPRM02] LÉVY B., PETITJEAN S., RAY N., MAILLOT J.: Least Squares Conformal Maps for Automatic Texture Atlas Generation. *ACM Trans. Graph. 21*, 3 (2002), 362–371. 10

[LS08] LOOP C., SCHAEFER S.: Approximating Catmull-Clark subdivision surfaces with bicubic patches. *ACM Trans. Graph. 27*, 1 (2008), 8. 5

[LSNC09] LOOP C., SCHAEFER S., NI T., CASTAÑO I.: Approximating Subdivision Surfaces with Gregory Patches for Hardware Tessellation. *ACM Trans. Graph. 28* (2009), 151:1–151:9. 6

[Mar95] MARUYA M.: Generating a Texture Map from Object-Surface Texture Data. *Computer Graphics Forum 14*, 3 (1995), 397–405. 12

[MBG*12] MARVIE J.-E., BURON C., GAUTRON P., HIRTZLIN P., SOURIMANT G.: GPU Shape Grammars. *Computer Graphics Forum 31*, 7 (2012), 2087–2095. 12

[MHTAM10] MUNKBERG J., HASSELGREN J., TOTH R., AKENINE-MÖLLER T.: Efficient Bounding of Displaced Bézier Patches. In *Proceedings of HPG'10* (2010), Eurographics Association, pp. 153–162. 18, 20, 21

[Mic09] MICROSOFT CORPORATION: Direct3D 11 Features, 2009. http://msdn.microsoft.com/en-us/library/ff476342(VS.85).aspx. 0, 1

[MNP08] MYLES A., NI T., PETERS J.: Fast Parallel Construction of Smooth Surfaces from Meshes with Tri/Quad/Pent Facets. *Computer Graphics Forum 27*, 5 (2008), 1365–1372. 6

[Mor01] MORETON H.: Watertight Tessellation using Forward Differencing. In *HWWS'01: Proceedings of the ACM SIGGRAPH/EUROGRAPHICS Workshop on Graphics Hardware* (2001), pp. 25–32. 8

[MYP08] MYLES A., YEO Y. I., PETERS J.: GPU Conversion of Quad Meshes to Smooth Surfaces. In *SPM '08: ACM Symposium on Solid and Physical Modeling* (2008), pp. 321–326. 6

[Nie13] NIESSNER M.: *Rendering Subdivision Surfaces using Hardware Tessellation*. Dr. Hut, 2013. 6, 22

[NL12] NIESSNER M., LOOP C.: Patch-Based Occlusion Culling for Hardware Tessellation. *CGI* (2012). 19, 20, 21

[NL13] NIESSNER M., LOOP C.: Analytic Displacement Mapping using Hardware Tessellation. *ACM Trans. Graph. 32*, 3 (2013), 26. 8, 13, 15, 22

[NLG12] NIESSNER M., LOOP C., GREINER G.: Efficient Evaluation of Semi-Smooth Creases in Catmull-Clark Subdivision Surfaces. *Computer Graphics Forum* (2012). 8

[NLMD12] NIESSNER M., LOOP C., MEYER M., DEROSE T.: Feature-adaptive GPU rendering of Catmull-Clark subdivision surfaces. *ACM Trans. Graph. 31*, 1 (2012), 6. 4, 6, 8, 14, 22

[NSSL13] NIESSNER M., SIEGL C., SCHÄFER H., LOOP C.: Real-time Collision Detection for Dynamic Hardware Tessellated Objects. In *Proc. EG'13* (2013). 21

[Nvi12a] NVIDIA: CUDA C Programming guide, 2012. 0

[Nvi12b] NVIDIA: NVIDIA's Next Generation CUDA Compute Architecture: Kepler GK110, 2012. http://www.nvidia.com/content/pdf/kepler/nvidia-kepler-gk110-architecture-whitepaper.pdf. 1

[Nvi13] NVIDIA: Kepler to Mobile, 2013. http://blogs.nvidia.com/blog/2013/07/24/kepler-to-mobile. 1, 22

[NYM*08] NI T., YEO Y. I., MYLES A., GOEL V., PETERS J.: GPU Smoothing of Quad Meshes. In *SMI '08: IEEE International Conference on Shape Modeling and Applications* (2008), pp. 3–9. 6

[PCK04] PURNOMO B., COHEN J. D., KUMAR S.: Seamless Texture Atlases. In *Proceedings of SGP'04* (2004), ACM, pp. 65–74. 10

[PEO09] PATNEY A., EBEIDA M., OWENS J.: Parallel View-Dependent Tessellation of Catmull-Clark Subdivision Surfaces. In *Proceedings of HPG* (2009), ACM, pp. 99–108. 1

[PG07] PAJAROLA R., GOBBETTI E.: Survey of Semi-Regular Multiresolution Models for Interactive Terrain Rendering. *The Visual Computer 23*, 8 (2007), 583–605. 11

[Pix12] PIXAR: OpenSubdiv, 2012. http://graphics.pixar.com/opensubdiv. 0, 6, 22

[Qua13] QUALCOMM: Qualcomm Technologies Announces Next Generation Qualcomm Snapdragon 805, 2013. http://www.qualcomm.com/media/releases/2013/11/20/qualcomm-technologies-announces-next-generation-qualcomm-snapdragon-805. 1, 22

[Rei97] REIF U.: A Refineable Space of Smooth Spline Surfaces of Arbitrary Topological Genus. *Journal of Approximation Theory 90*, 2 (1997), 174–199. 13, 14

[RNLL10] RAY N., NIVOLIERS V., LEFEBVRE S., LEVY B.: Invisible Seams. *Computer Graphics Forum (Proc. EGSR'10) 29*, 4 (2010), 1489–1496. 10

[SA12] SEGAL M., AKELEY K.: The OpenGL Graphics System: A Specification (Version 4.0 (Core Profile), Mar. 2012. http://www.opengl.org/registry/doc/glspec40.core.20100311.pdf. 1

[SAE93] SHIRMUN L., ABI-EZZI S. S.: The Cone of Normals Technique for Fast Processing of Curved Patches. *Computer Graphics Forum 12*, 3 (1993), 261–272. 17, 19, 21

[SBOT08] SHOPF J., BARCZAK J., OAT C., TATARCHUK N.: March of the Froblins: Simulation and Rendering Massive Crowds of Intelligent and Detailed Creatures on GPU. In *ACM SIGGRAPH 2008 classes* (2008), ACM, pp. 52–101. 20

[Sch12] SCHWARZ M.: Practical Binary Surface and Solid Voxelization with Direct3D11. In *GPU Pro3: Advanced Rendering Techniques*. AK Peters Limited, 2012, p. 337. 21

[SGSH02] SANDER P. V., GORTLER S. J., SNYDER J., HOPPE H.: Signal-Specialized Parametrization. In *Proc. EGWR'02* (2002), pp. 87–98. 11

[SH02] SHEFFER A., HART J. C.: Seamster: Inconspicuous Low-Distortion Texture Seam Layout. In *VIS'02* (2002), IEEE Computer Society, pp. 291–298. 10

[SKN*14] SCHÄFER H., KEINERT B., NIESSNER M., BUCHENAU C., GUTHE M., STAMMINGER M.: Real-time deformation of subdivision surfaces from object collisions. In *Proceedings of the 6th High-Performance Graphics Conference* (2014), EG. 16

[SKNS14] SCHÄFER H., KEINERT B., NIESSNER M., STAMMINGER M.: Local painting and deformation of meshes on the gpu. *Computer Graphics Forum* (2014). 15

[SKS13] SCHÄFER H., KEINERT B., STAMMINGER M.: Real-Time Local Displacement using Dynamic GPU Memory Management. In *Proceedings of HPG'13* (2013), pp. 63–72. 15

[SKU08] SZIRMAY-KALOS L., UMENHOFFER T.: Displacement Mapping on the GPU - State of the Art. *Computer Graphics Forum 27*, 6 (2008), 1568–1592. 9

[SM88] SEDERBERG T., MEYERS R.: Loop Detection in Surface Patch Intersections. *Computer Aided Geometric Design 5*, 2 (1988), 161–171. 18, 19, 21

[SNK*14] SCHÄFER H., NIESSNER M., KEINERT B., STAMMINGER M., LOOP C.: State of the art report on real-time rendering with hardware tessellation. 1

[SPM*12] SCHÄFER H., PRUS M., MEYER Q., SÜSSMUTH J., STAMMINGER M.: Multi-Resolution Attributes for Hardware Tessellated Meshes. In *Proceedings of I3D'12* (2012), ACM, pp. 175–182. 12, 13

[SPM*13] SCHÄFER H., PRUS M., MEYER Q., SÜSSMUTH J., STAMMINGER M.: Multi-Resolution Attributes for Hardware Tessellated Objects. *IEEE Transactions on Visualization and Computer Graphics* (2013), 1488–1498. 15

[SRK*15] SCHÄFER H., RAAB J., KEINERT B., MEYER M., STAMMINGER M., NIESSNER M.: Dynamic feature-adaptive subdivision. In *Proceedings of the 19th Symposium on Interactive 3D Graphics and Games* (2015), ACM, pp. 31–38. 8

[SS09] SCHWARZ M., STAMMINGER M.: Fast GPU-based Adaptive Tessellation with CUDA. *Computer Graphics Forum 28*, 2 (2009), 365–374. 1

[Sta98] STAM J.: Exact Evaluation of Catmull-Clark Subdivision Surfaces at Arbitrary Parameter Values. In *Proceedings of SIGGRAPH* (1998), Annual Conference Series, ACM, pp. 395–404. 5

[Sti80] STINY G.: Introduction to Shape and Shape Grammars. *Environment and Planning B 7*, 3 (1980), 343–351. 11

[SWB98] SLOAN P.-P. J., WEINSTEIN D. M., BREDERSON J.: Importance Driven Texture Coordinate Optimization. *Computer Graphics Forum 17*, 3 (1998), 97–104. 11

[SWG*03] SANDER P. V., WOOD Z., GORTLER S. J., SNYDER J., HOPPE H.: Multi-Chart Geometry Images. In *Proceedings of SGP'03* (2003), pp. 146–155. 10

[Tat09] TATARCHUK N.: Fast High-Quality Rendering with Real-Time Tessellation on GPUs. In *ShaderX 7*, Engel W., (Ed.). Charles River Media, 2009. 15

[TBB10] TATARCHUK N., BARCZAK J., BILODEAU B.: Programming for Real-Time Tessellation on GPU. AMD whitepaper 5, 2010. 11

[THCM04] TARINI M., HORMANN K., COGNONI P., MONTANI C.: PolyCube-Maps. *ACM Trans. Graph. 23*, 3 (2004), 853–860. 16

[TMJ98] TANNER C. C., MIGDAL C. J., JONES M. T.: The Clipmap: A Virtual Mipmap. In *Proceedings of SIGGRAPH 98* (1998), Annual Conference Series, ACM, pp. 151–158. 11

[Ulr02] ULRICH T.: Rendering Massive Terrains using Chunked Level of Detail Control. In *ACM SIGGRAPH 02 Talks* (2002), ACM, p. 34. 11

[VPBM01] VLACHOS A., PETERS J., BOYD C., MITCHELL J. L.: Curved PN Triangles. In *Proceedings of I3D'01* (2001), pp. 159–166. 5

[Wil83] WILLIAMS L.: Pyramidal Parametrics. *Computer Graphics 17*, 3 (1983), 1–11. 12, 13

[WMWF07] WATSON B., MÜLLER P., WONKA P., FULLER A.: Urban Design and Procedural Modelling. In *ACM SIGGRAPH 2007 Courses* (2007). 11

[XGH*11] XIA J., GARCIA I., HE Y., XIN S.-Q., PATOW G.: Editable Polycube Map for GPU-based Subdivision Surfaces. In *Proceedings of I3D'11* (2011), ACM, pp. 151–158. 16

[YBP12] YEO Y. I., BIN L., PETERS J.: Efficient Pixel-Accurate Rendering of Curved Surfaces. In *Proceedings of I3D'12* (2012), pp. 165–174. 8

[YBP14] YEO Y. I., BHANDARE S., PETERS J.: Efficient pixel-accurate rendering of animated curved surfaces. In *Mathematical Methods for Curves and Surfaces*. Springer, 2014, pp. 491–509. 8

[YS11] YUSOV E., SHEVTSOV M.: High-Performance Terrain Rendering Using Hardware Tessellation. *WSCG* (2011). 11

[Yus12] YUSOV E.: Real-Time Deformable Terrain Rendering with DirectX 11. In *GPU Pro 3*, Engel W., (Ed.). A K Peters, 2012. 15